

Xenon Trapping in Metal-Supported Silica Nanocages

Y. Xu, A. R. Head

To be published in "Small"

August 2021

Center for Functional Nanomaterials
Brookhaven National Laboratory

U.S. Department of Energy
USDOE Office of Science (SC), Basic Energy Sciences (BES) (SC-22)

Notice: This manuscript has been authored by employees of Brookhaven Science Associates, LLC under Contract No. DE-SC0012704 with the U.S. Department of Energy. The publisher by accepting the manuscript for publication acknowledges that the United States Government retains a non-exclusive, paid-up, irrevocable, world-wide license to publish or reproduce the published form of this manuscript, or allow others to do so, for United States Government purposes.

DISCLAIMER

This report was prepared as an account of work sponsored by an agency of the United States Government. Neither the United States Government nor any agency thereof, nor any of their employees, nor any of their contractors, subcontractors, or their employees, makes any warranty, express or implied, or assumes any legal liability or responsibility for the accuracy, completeness, or any third party's use or the results of such use of any information, apparatus, product, or process disclosed, or represents that its use would not infringe privately owned rights. Reference herein to any specific commercial product, process, or service by trade name, trademark, manufacturer, or otherwise, does not necessarily constitute or imply its endorsement, recommendation, or favoring by the United States Government or any agency thereof or its contractors or subcontractors. The views and opinions of authors expressed herein do not necessarily state or reflect those of the United States Government or any agency thereof.

Xenon Trapping in Metal-Supported Silica Nanocages

Yixin Xu, Matheus Dorneles de Mello Chen Zhou, Shruti Sharma, Burcu Karagoz, Ashley Head, Zubin Darbari, Iradwikanari Waluyo, Adrian Hunt, Dario J. Stacchiola, Sergio Manzi, Alejandro M. Boscoboinik, Victor D. Pereyra and J. Anibal Boscoboinik**

Y. Xu, C. Zhou, Z. Darabi, Dr. J. A. Boscoboinik
Materials Science and Chemical Engineering Department, State University of New York at Stony Brook, 100 Nicolls Rd, Stony Brook, New York, 11794, USA

Y. Xu, Dr. M. D. Mello, C. Zhou, Dr. B. Karagoz, Dr. A. Head, Z. Darbari, Dr. D. J. Stacchiola, Dr. J. A. Boscoboinik
Center for Functional Nanomaterials, Brookhaven National Laboratory, 735 Brookhaven Ave, Upton, New York, 11973, USA
E-Mail:mdorneles@bnl.gov; jboscoboinik@bnl.gov

Dr. M. D. Mello, Dr. J. A. Boscoboinik
Catalysis Center for Energy Innovation, University of Delaware, Newark, Delaware, 19716, USA

Dr. S. Sharma
Advanced Energy Research and Technology Center, State University of New York at Stony Brook, 1000 Innovation Road, Stony Brook, New York, 11794, USA

Dr. I. Waluyo, Dr. A. Hunt
National Synchrotron Light Source II, Brookhaven National Laboratory, 743 Brookhaven Avenue, Upton, New York, 11967, USA

Dr. S. Manzi
Departamento de Física, Instituto de Física Aplicada (INFAP) - CONICET, Universidad Nacional de San Luis, Chacabuco 917, San Luis 5700, Argentina

Dr. A. M. Boscoboinik
Department of Mechanical Engineering and Applied Mechanics, University of Pennsylvania, Pennsylvania, USA

Dr. V. D. Pereyra
Departamento de Física, Instituto de Matemática Aplicada (IMASL) - CONICET, Universidad Nacional de San Luis, Chacabuco 917, San Luis 5700, Argentina

Keywords: xenon trapping, silica nanocage, synchrotron AP-XPS, DFT calculation, Monte Carlo simulation

Abstract: Xenon is a valuable and scarce noble gas used in various applications, including lighting, electronics, and anesthetics, among many others. It is also a volatile byproduct of the nuclear fission of uranium. We present a novel material architecture consisting of silicate nanocages in contact with a metal surface and an approach for trapping single Xe atoms in these cages. The trapping is done at low Xe pressures and temperatures between 400 K and 600 K, and the process is monitored *in situ* using synchrotron-based ambient pressure X-ray photoelectron spectroscopy (AP-XPS). Release of the Xe from the cages occurs only when heating to temperatures above 750 K. A model that explains the experimental trapping kinetics is proposed and tested using Monte Carlo methods. Density functional theory calculations show activation energies for Xe exiting the cages consistent with experiments. This work can have significant implications in various fields, including Xe production, nuclear power, nuclear waste remediation, and non-proliferation of nuclear weapons. The results are also expected to apply to Ar, Kr, and Rn, opening an even more comprehensive range of applications.

1. Introduction

Xenon is a generally unreactive noble gas with high demand in various fields. It is typically produced using an energy-intensive process known as cryogenic distillation[1] and used as a light source in high-intensity discharge (HID) lamps,[2] in bactericidal lamps,[3] in ion propulsion systems,[4] and as an anesthetic.[5] It has also been proposed as an extreme-ultraviolet (EUV) radiation source for next-generation photolithography.[6] Its low concentration in the atmosphere and the energy cost of purification make Xe expensive.[7] Predictions have shown that Xe should be more abundant than other noble gases like argon (Ar) and krypton (Kr) based on studies with meteorites. However, Xe's concentration in the earth's crust and the

atmosphere are much lower than predicted. This phenomenon is known as the “missing Xenon paradox”. [8] Finding efficient ways to trap and separate it from other gases can have important implications.

Additionally, there is particular interest from the nuclear energy industry in finding ways to control the release of Xe, which is generated during the nuclear fission of uranium. Its presence in nuclear fuel rods was partially responsible for the Chernobyl accident. [9] Also related to its release during nuclear fission, its detection at elevated levels in the open air can be a sign of a nuclear weapons test. [10]

Significant effort has been devoted to improving Xe production by an adsorption-based approach. Many porous materials, including activated carbon, K strolith® 4AK zeolite [11], zinc tetrozolate framework [12], and some other zeolites and metal-organic frameworks [13-16] have demonstrated adsorption for this application at room temperature. More recently, a combination of AgX zeolite adsorbent and cryogenic distillation was shown to benefit Xe production in the industry [17]. However, adsorption using the aforementioned materials is based on equilibrium concentrations between the material and the gas phase. This equilibrium-based (reversible) separation makes them challenging to use for low Xe concentration applications. There are also concerns regarding the selectivity and purity of the gas recovered in the co-adsorption of other species such as oxygen, nitrogen, and hydrocarbons [17]. The latter raises safety concerns during the gas recovery step (desorption by heating) since hydrocarbons can form explosive mixtures above determined concentrations. Therefore, it is of particular interest to find new materials and approaches selective only to noble gases.

Prior studies on two-dimensional (2-D) silicate bilayers grown on metal supports showed that these structures could irreversibly trap all noble gases larger than Ne [18, 19] at room

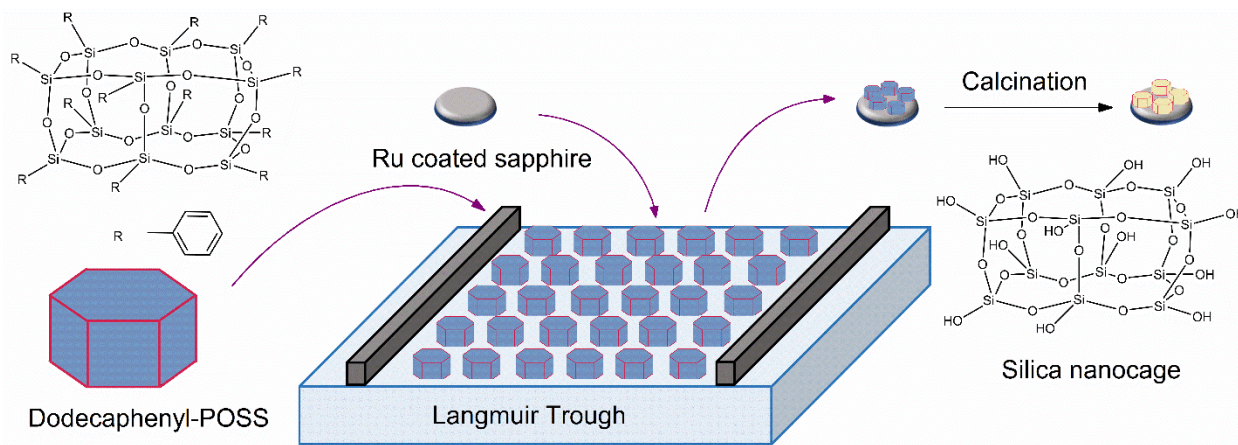
temperature. The noble gas atoms were trapped within hexagonal prism-shaped silicate nanocages in the structure. They could then be selectively released by heating the materials to different temperatures depending on the gas under study (Ar: 348 K, Kr: 498 K, Xe: 673 K, Rn: 775 K). However, the synthesis of such silicate bilayers is prohibitively expensive and time-consuming for practical purposes.[20] Since the hexagonal prism silicate nanocage in contact with a metal is responsible for the trapping, one could envision an alternative structure having those same building blocks. In a way, the material synthesis could be scaled up using established high surface area coating processes.[21] A commercially available hexagonal prism silica nanocage called dodecaphenyl-polyhedral oligomeric silsesquioxane (Dodecaphenyl-POSS[22], D-POSS) is shown at the top left of **Scheme 1**. Each of the twelve vertices of the cage is terminated by a phenyl group. In this work, we produce a material using D-POSS cages supported on a thin ruthenium film to explore its behavior toward Xe trapping. After a sequence of activation treatments of the material, we show the successful trapping of Xe using ambient pressure X-ray photoelectron spectroscopy (AP-XPS). We then develop a model to explain mechanistic aspects of the trapping process by combining experimental, theoretical, and simulation tools.

2. Results and discussion

2.1. Nanocages deposition

D-POSS molecules were deposited on Ru coated sapphire wafers (**Figure S1**) using a Langmuir trough (Scheme 1). The synthesis details are described in the Methods section and the SI (**Figure S2**). After deposition, the film was calcined to burn the organic moieties from the POSS

molecules. Atomic force microscopy (AFM) images of the Ru film were taken before and after deposition of nanocages and associated treatments (**Figure S3**). In both cases, a granular morphology with domains in the order of ~ 50 nm is observed, with height variations of ~ 3 nm on and off these domains. The unchanged morphology indicates no significant structural changes on the Ru film upon deposition of the cages and subsequent calcination. XPS confirmed the presence of Si on the surface, with an estimated coverage of 42%, as shown in **Figure S4** and **Table S1**. Further characterization of the material by infrared reflection absorption spectroscopy and Raman spectroscopy is shown in the SI. The vibrational spectroscopy results indicate that while the silicate nanocage structure is preserved upon calcination, these are likely oligomerized to form extended structures without long-range order on the Ru surface.



Scheme 1. Schematic of the approach to deposit silica nanocages on the Ru film, using a Langmuir trough. The deposited cages are calcined after the deposition to remove the organic component.

2.2. Influence of the chemical state of Ru in Xe trapping

In this section, we demonstrate that the D-POSS cages can trap Xe, and we show that the chemical state of Ru plays a critical role in the trapping. The sample was exposed to 1 Torr of Xe at 420 K while illuminating with X-rays (983 eV) for 20 min. After evacuating the Xe gas, Xe

$3d_{5/2}$ and Ru $3d$ spectra were collected (red spectra in **Figure 1a** and **1b**, respectively). No Xe is observed in the spectrum, while the Ru $3d$ spectrum shows peaks at 284.9 and 280.9 eV and a broad feature below 283 eV, characteristic of oxidized ruthenium[23] (Figure 1b). Ru oxidation results from the calcination step to remove the organic ligands from the nanocages. Ru is then reduced by exposure to 0.1 Torr of H_2 at 723 K for ~60 min, followed by a second attempt at the same trapping conditions. The complete reduction of Ru to the metallic state is verified by XPS, as shown in the black spectrum in Figure 1b. A peak at ~669.5 eV (black spectrum in Figure 1a), corresponding to the Xe $3d_{5/2}$ core level, indicates the successful trapping of Xe. These observations indicate that having Ru in the metallic state is necessary for the nanocages to trap Xe. The O $1s$ and Si $2p$ spectra corresponding to these experiments can be found in the SI (**Figure S6**). The O $1s$ spectra in Figure S6a show that the component corresponding RuO_x disappears upon treatment with H_2 , supporting that Ru is fully reduced. Additionally, the O $1s$ components corresponding to Ru-O-Si and chemisorbed O get significantly reduced in area. At the same time, no change is observed in the component associated with the Si-O-Si linkages in the cage. The Si $2p$ peak slightly shifts towards higher binding energy and decreases in full-width at half maximum due to the reduction of Ru-O-Si. None of these changes are indicative of structural modification of the cages.[24]

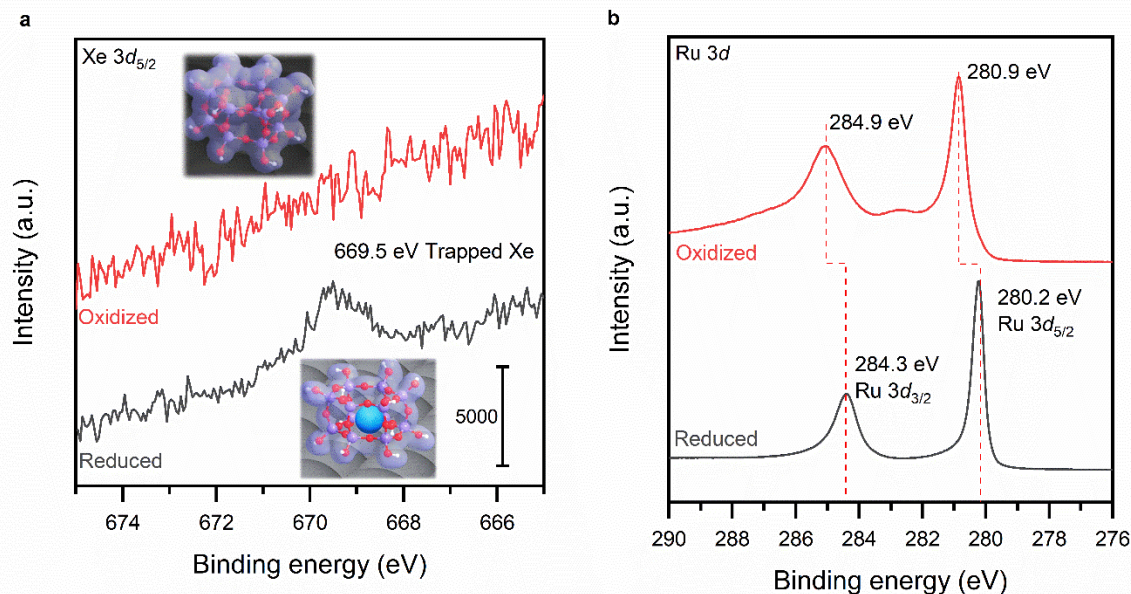


Figure 1. Effect of the chemical state of Ru on the Xe trapping. XPS spectra of (a) Xe $3d_{5/2}$ and (b) Ru $3d$ core levels, both experiments of “As synthesized” (red) and “H₂ treated” (black), are taken in the same UHV environment after exposure to 1 Torr of Xe gas in the presence of X-rays. The insets in (a) illustrate an empty nanocage on an oxidized Ru surface (upper cartoon) and a Xe-filled cage on a metallic Ru surface (lower cartoon).

The results are consistent with what was reported for gas trapping in silicate bilayer systems, in which the polygonal prism silica cages form a 2D material on a Ru(0001) crystal.[19] For bilayer silicates, it was concluded that the mechanism of noble gas trapping consists of the following steps: (i) Noble gas cations are produced as part of the XPS measurements, as the X-rays remove electrons from the neutral gas species; (ii) Cations enter the cage; (iii) Cations are neutralized by electron transfer from neighboring species, most likely the Ru metal; and (iv) The neutral species are stable inside of the cage, and the “uncaging” or “release” process has considerable activation energies. The current finding that Xe is trapped only when metallic Ru is present is evidence that the electron that neutralizes the noble gas cation (in step iii above) must come from the metal and not the silicate cage.

The films produced here have a heterogeneous coverage distribution of silicate cages on the surface, as evidenced by variations in the Si $2p$ /Ru $3d_{5/2}$ peaks area ratios across the sample. To assess if this has any effect on the trapping of Xe, we repeated the same trapping experiments in three locations with different populations of silicate nanocages (**Figure S7**). The results show a linear correlation between Xe trapped and Si present (a proxy for the population of nanocages).

2.3. Trapping experiments

To study the kinetics of the trapping process, we collected XP spectra under 1 Torr of Xe at three different temperatures. **Figure 2a** shows the [Xe $3d_{5/2}$ /Ru $3d_{5/2}$] peak area ratio, as a function of time, at 420, 480, and 600 K, normalized to 1. This normalized peak area ratio is proportional to the amount of trapped Xe. Trapping increases rapidly with time up to 30 min at all temperatures. It reaches saturation after 50 min for 480 K. For the 420 K case, the coverage approaches saturation closer to 70 min. However, at 600 K, significantly less Xe is trapped. After 50 min, only 20% of the saturation coverage is reached. Initial trapping rates are calculated based on the normalized peak area ratio, shown in **Table S2**. It is evident that the trapping rate at 480 K is higher than at 420 K and decreases significantly at 600 K.

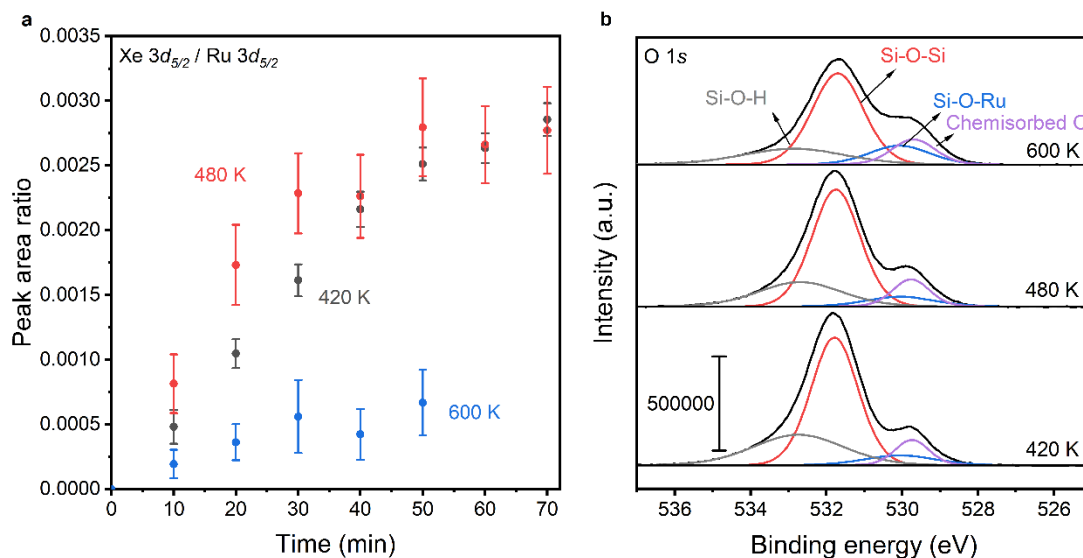


Figure 2. (a) Xe trapping kinetics. Xe $3d_{5/2}$ / Ru $3d_{5/2}$ peak area ratio vs. time at 420, 480, and 600 K; (b) O $1s$ region at these temperatures in UHV after evacuating Xe; the fitted components are: chemisorbed O on the Ru substrate (purple curve, 529.8 eV), O bonded to Ru and silicon (Si-O-Ru, blue curve, 530.1 eV), O in silica cage involved in Si-O-Si bonds (red curve, 531.8 eV), and Si-OH groups (gray curve, 532.7 eV).

Moreover, the spectra for the other elements also reveal changes caused by heating the material. The O $1s$ spectra in **Figure 2b** can be fitted into four species. The main peak located at 531.8 eV is attributed to O in silica cages. At 530.1 and 529.8 eV, two peaks are attributed to O in Si-O-Ru bonds and chemisorbed O on Ru, respectively.[25] The broad peak at 532.7 eV is assigned to terminal Si-OH groups. [26, 27] Peak intensities at 420 K and 480 K do not show any changes. However, at 600 K, the shoulder peak corresponding to Si-O-Ru (blue curve in Figure 2b at around 530.1 eV) increases in intensity, suggesting the formation of more Si-O-Ru bonds upon heating and a decrease in the contribution of the Si-OH peak (Areas of the O $1s$ region relative to Ru $3d_{5/2}$ are shown in Table S2).

We further investigated the reversibility and reusability of the material (**Figure S9**) by comparing the [Xe $3d_{5/2}$ /Ru $3d_{5/2}$], [Si $2p$ /Ru $3d_{5/2}$], and [O $1s$ /Ru $3d_{5/2}$] peak area ratios after Xe saturation at two different conditions. The data suggest consecutive trapping experiments separated by an anneal step to remove trapped Xe yields similar amounts of trapped gas.

2.4. Release experiments

The Xe release from the nanocages was followed by monitoring the Xe $3d_{5/2}$ core level spectra as a function of temperature in UHV. The Ru $3d_{5/2}$ core level area was used as a reference to account for any area changes related to temperature. The [Xe $3d_{5/2}$ /Ru $3d_{5/2}$] peak area ratios (normalized to the initial area ratio) are presented as a function of temperature in **Figure 3a**. Xe is released in two regimes during the experiment. The first one occurs between 450 and 550 K, representing about 35 % of the trapped Xe. It is attributed to Xe being released from the interface between the nanocage and Ru, similar to silica bilayers[19]. The second (and faster) occurs above 750 K, corresponding to Xe trapped inside the nanocages. This data shows that Xe atoms trapped in the silica nanocages prepared in this work are more stable than those trapped in the nanocages of bilayer silicates. The latter are released at lower temperatures (673 K).[19]

We further explored the changes in the O $1s$ speciation with temperature, as presented in **Figure S10**. The total amount of O decreases when flash-annealing to high temperatures. However, heating increases Si-O-Ru, starting from 550 K, as observed during the trapping experiment (**Figure S10**). On the other hand, the Si $2p$ peak area does not change.

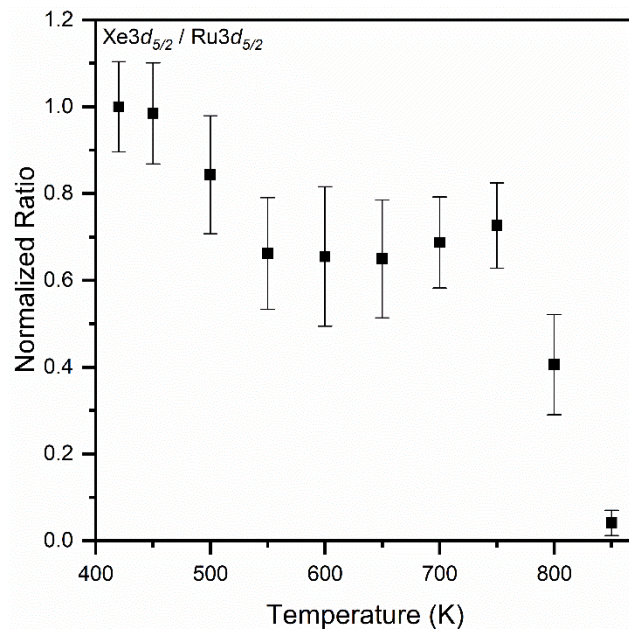


Figure 3. Xe release data after trapping at 420 K. Normalized peak area ratio Xe $3d_{5/2}$ / Ru $3d_{5/2}$ after heating to different temperatures.

Even though this work focuses mainly on Xe, the same mechanism is expected to apply to the trapping of other noble gases, including Ar, Kr, and Rn, based on comparison with prior work on bilayer silicates. The different thermal stability of Ar, Kr, Xe, and Rn can improve trapping selectivity in separation processes. Prior experiments in our group have shown that other gases typically present in mixtures, such as O₂ and N₂, do not get trapped in the cages (data not shown).

2.5. Kinetic Model for Xenon Trapping

In order to interpret the non-Arrhenius behavior in the trapping kinetics observed experimentally, a trapping model was developed and tested using a combination of kinetic Monte Carlo methods and molecular dynamics simulations. As discussed above, the trapping process consists of at least three steps: 1. Xe ionization ($\text{Xe}^0 \rightarrow \text{Xe}^+$), 2. Xe^+ entering the cage, and 3. neutralization of cations ($\text{Xe}^+ \rightarrow \text{Xe}^0$) inside the cage, resulting in trapping.[19] When trying to understand

kinetics, these three steps need to be considered. A constant Xe^+ population is expected during the experiment considering a constant pressure of Xe and a constant flux of X-rays. However, the following step, that of cations entering the cage, will depend on (i) the temperature T of the sample, (ii) the kinetic energy KE^+ of the gas phase cations, and (iii) the fraction of cages already occupied θ_{Xe} , where we define that $\theta_{\text{Xe}}^{\text{max}} = 1$ when saturation is reached at $T=480$ K.

For the Xe^+ to enter the cage, the cage opening must be large enough. In this model, an activated process is considered. The probability P_o that a cage opening is large enough for a cation to enter is given by **Equation 1**:

$$P_o = A \cdot \exp\left(-\frac{E_{app}}{k_B T}\right) \quad (1)$$

where A is a pre-exponential factor, k_B is Boltzmann constant, E_{app} is the activation energy needed for the cage to open large enough, and T is the sample's temperature. Two kinetic Monte Carlo schemes are used in conjunction to simulate the experimental data.[28-30] The first one is carried out following the steps outlined below.

The time step dt between cage opening events follows a Poisson distribution and is given by **Equation 2**:

$$dt = -\ln(\zeta)/P_o, \quad (2)$$

Where ζ is a random number uniformly distributed between 0 and 1.

In order to obtain reasonable statistics, we consider 10^6 cages, and we choose a time interval Δt ($\Delta t \gg dt$) such that each cage opens approximately 10^7 times. Then, one can obtain the frequency f as the number of times (n) in which each cage opens during the time interval Δt , as $f = n/\Delta t$.

Molecular dynamics (MD) simulations of a vibrating cage were used to estimate the energy barrier of cages opening. The modeled structure consists of a hexagonal prism silicate nanocage

sitting on a Ru(0001) surface (as shown in **Figure 4a**), in which a Xe cation could attempt to enter. The distance between Si atoms at opposite sides of the hexagon in the cage was tracked in the MD simulations. This distance was used as a proxy to follow the cage expansion and contraction with time (at different temperatures, **Figure 4b**). As the temperature increases, the cage opening oscillates at a higher frequency. An Arrhenius plot was generated with the frequency values and the temperature, allowing the estimation of an activation energy of 0.043 eV for the opening process (**Figure S11** in the SI). This value serves as an upper limit for the energy barrier for the trapping process.

We can now obtain the probability distribution for the cage opening event for each T . **Figure 4c** shows an example of such probability distributions at different temperatures considering an E_{app} of 0.043 eV. The probability distribution is plotted as a function of f/f_{Xe} , where f_{Xe} is a constant that depends on the frequency at which Xe^+ attempts to enter the cage and its temperature. As expected, the maximum of the distribution shifts to higher frequencies at higher temperatures. These probability distributions are then used to run a second kinetic Monte Carlo simulation to model the Xe trapping process.[28, 30, 31] A flow diagram for the simulation is shown in the supporting information (**Scheme S1**). Briefly, an array of 10^6 empty cages is defined. A nanocage is randomly chosen, and its frequency (f) is obtained based on the probability distribution described above. Then, a Xe trapping event is attempted. The event is successful (the cage is filled) if the frequency f of the randomly chosen cage is within a tolerance parameter (Tol) of the value of the constant f_{Xe} (i.e., $|f - f_{Xe}| < Tol$). After each trapping attempt, the time increment dt' is calculated by **Equation 3**, where θ_{Xe} is the fraction of cages occupied by Xe.

$$dt' = -\frac{\ln \zeta}{(1 - \theta_{Xe})f_{Xe}} \quad (3)$$

The experimental data for the trapping kinetics at three different temperatures are shown as filled circles in **Figure 4d** and compared to the Monte-Carlo simulations (solid lines). While the agreement is remarkable, the simulation results are highly correlated to the *Tol* parameter. For example, in the case of Figure 4d, for $E_{app} = 0.043$ eV, the *Tol* parameter needs to be set to 17 %, i.e., the frequency f has to be within 17% of the constant f_{Xe} ($f_{Xe}/A = 7.35 \times 10^{-7} \pm 1.263 \times 10^{-7}$) for a trapping attempt to be successful. We then screened different values for the energy barrier for trapping, ranging from 0.0043 eV to 0.043 eV (obtained by MD calculations as the frequency of cage vibrations).

The probability distributions are shown in **Figure S12**. As we decrease E_{app} , the tolerance needed for accepting an event also decreases. For $E_{app} = 0.0043$ eV, the *Tol* needed is less than 0.2% to f_{Xe} , while for higher values of E_{app} , for example, with $E_{app} = 0.015$ eV, the needed *Tol* is less than 5%. Values of tolerance and f_{Xe} at different E_{app} can be found in Figure S12f. Other factors may decrease the actual value of E_{app} , like the dipole created between the charge of the cation and the electrons on the metal surface. That dipole could facilitate the cation entrance in the cage even at openings that do not precisely match the frequency of Xe cations hitting the cage surface.

Further comparison between calculations and experimental data is possible by estimating rate constants for trapping at different temperatures. For the experimental data, first-order kinetics is assumed according to **Equation 4**.

$$d\theta_{Xe}/dt = k(1 - \theta_{Xe}) \quad (4)$$

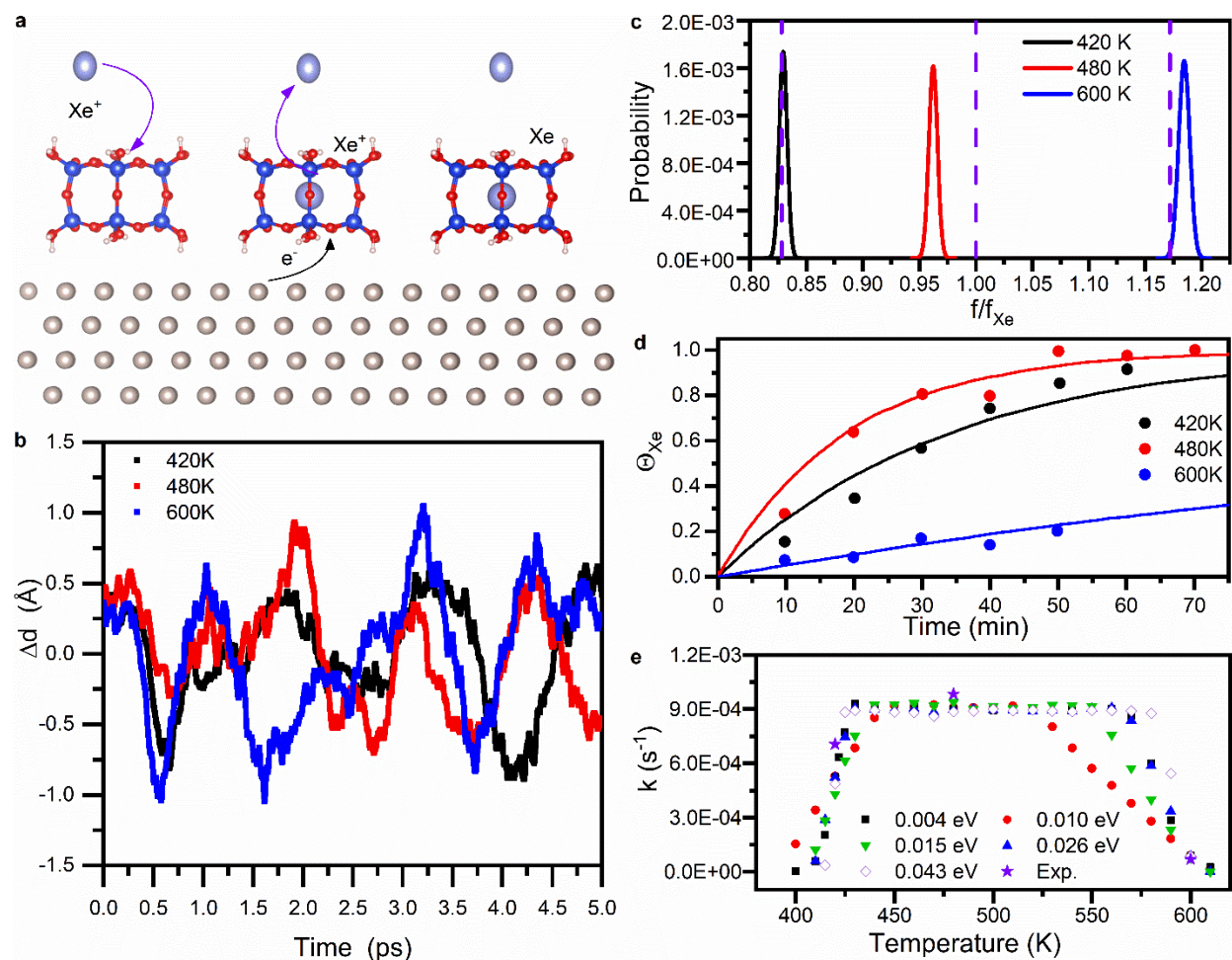


Figure 4. (a) Schematic illustration of the Xe⁺ trapping process by silicon nanocages supported on a Ru surface. Color code: Si (blue), O in silica films (red), H (light gray) Ru (silver), and Xe (purple); (b) Difference in distances between opposite Silicon atoms in the nanocages obtained by molecular dynamics simulations of Si nanocages vibrating at different temperatures; (c) Probability distribution of cages opening at different temperatures with an activation energy of $E_{app} = 0.043$ eV; (d) Fitting of the experimental data by using estimated parameters from the Monte Carlo simulations ($E_{app} = 0.043$ eV, $f_{Xe}/A = 7.35e-7 \pm 1.263e-7$); (e) Simulated rate constants from Monte Carlo compared to experimental data. Each value of E_{app} has an associated tolerance value that can be found in **Figure S12f**.

Fitting the experimental data yields the rate constant, k , at each temperature. These are displayed in **Figure 4e** as violet stars. However, for practical applications, the temperature with the maximum trapping rate is desired. Therefore, more MC simulations were performed considering

a wide range of temperatures and E_{app} values. The rate constants obtained from the simulations are also shown in Figure 4e.

Interestingly, there is a range of optimal temperatures yielding a maximum value of k rather than a single best temperature. A range of E_{app} values agrees with the experimental data and with that obtained from the MD simulations and even lower barriers down to 0.0043 eV. More experimental data in the temperature range between 535 K and 575 K would be needed to narrow the E_{app} value by comparing experiments and MC simulations.

2.6. Density Functional Theory Calculations

The experimental trapping and release data highlight interesting features observed for the nanocages compared to the silicate bilayers in prior work[19]. Therefore, DFT calculations were performed to probe the structure changes upon Xe trapping. Several parameters were used to track the changes upon trapping, as illustrated in **Figure S13**: (i) distance between Ru atoms at the interface and bulk (Ru_i-Ru_b); (ii) interface distance; (iii) distance between opposite Si atoms on top ($Si_t - Si_t$), and bottom ($Si_b - Si_b$) faces; (iv) distances between opposite O atoms on top ($O_t - O_t$), middle (O_m-O_m), and bottom ($O_b - O_b$). The data is reported in **Table S3**. In the configuration evaluated, the distance changes (Δd) between pairs of opposite atoms show that the cage expands to accommodate the Xe atom inside; positive Δd values indicate expansion, while negative values indicate compression. The extent to which this expansion occurs is similar to that reported for the silicate bilayers. For example, the nanocages show a $\Delta d(Si-Si)$ of about -0.08 \AA for four of the six Si-Si opposite pairs compared to -0.03 \AA for the bilayer. A similar observation can be made for the $\Delta d(O_m-O_m)$, which shows -0.19 \AA for the nanocage over 0.21 \AA for the bilayer.[19] Notably, the nanocage is elongated in one direction, unlike the silicate bilayers with

symmetric hexagonal prisms. The $\Delta d(\text{O}_m\text{-O}_m)$ values are for oxygen atoms opposite from each other across the plane of symmetry (see Figure S13). Adsorption, trapping, and release energies were calculated and are presented in **Figure 5a**. Adsorption energies are defined as the energy required for the gas atom to be physisorbed outside the cage, according to **Equation 5**.

$$\Delta E_{ads} = E_{sub+gas^*} - (E_{gas} + E_{sub}), \quad (5)$$

$E_{sub+gas^*}$ is the total energy for the adsorbed system of Xe* inside the nanocage on Ru(0001). E_{sub} and E_{gas} are the total energy of the noninteracting individual components of the nanocage on Ru(0001) and the isolated Xe atom, respectively. The calculated ΔE_{ads} is -0.34 eV for the cage, which is the same order of magnitude observed for Xe adsorbed on the silica bilayers.[19] The energy required to trap Xe (ΔE_{trap}) is defined as the energy difference of the optimized structure with and without Xe inside the nanocage. A ΔE_{trap} of 0.65 eV indicates that having the noble gas inside the cage is less thermodynamically favorable than having it physisorbed. We further determined the energetics of a trapping pathway using the climbing image nudged elastic band (CI-NEB) method[32] for neutral noble gas atoms. As expected, there is a considerable expansion of the cage to accommodate the atom entering it. The calculated trapping energy barrier (E_{app}) is 3.02 eV, while the release energy barrier (E_{rel}) is 2.36 eV. Note that the calculated energy barriers are for neutral Xe atoms, while xenon enters the cage as a cation in the experiments. That is why the kinetic Monte Carlo simulations indicate much lower energies for the trapping process to occur. The energy barriers (both trapping and release) from DFT for the silica nanocages are higher than those obtained for the silica (and aluminosilicate) bilayers, which were $E_{app} = 2.52$ eV and $E_{rel} = 1.94$ eV. This suggests that for the flat cage configurations, the release of Xe requires higher energy than from the bilayers, which is consistent with the higher temperatures required for the Xe release from single cages shown in Figure 3.

The Xe release energy barrier obtained from DFT calculations was then used to simulate the desorption experiment from Figure 3 by assuming a first-order reaction law. The rate constants were calculated according to the Arrhenius equation (more details can be found in the SI). The calculated apparent Gibbs free energy for the flat cage agrees well with the experimental release data at high temperatures, predicting only slightly higher release temperatures (**Figure S15**). However, these calculations cannot explain the Xe release at lower temperatures. The lower temperature range, representing about 35 % of the released Xe, fits well with an energy barrier of about 1.27 eV. Another location where the trapping/release of Xe can occur is the interface between the nanocage and the metal surface, which is explored next (see **Figure 5b**). In this configuration, a Xe cation enters from the sides, under the cage, being stabilized by transferring an electron from the metallic Ru.

Energy barriers determined for such a system show lower trapping (1.63 eV) and release (1.27 eV) barriers. Simulated TPD data based on these calculated barriers show a good agreement with the experimental data (Figure S15), which slightly underpredicts the low-temperature release curve. Calculated Xe $3d_{5/2}$ binding energies (**Table S5**) show that Xe trapped in the nanocage and at the interface cannot be distinguished by XPS.

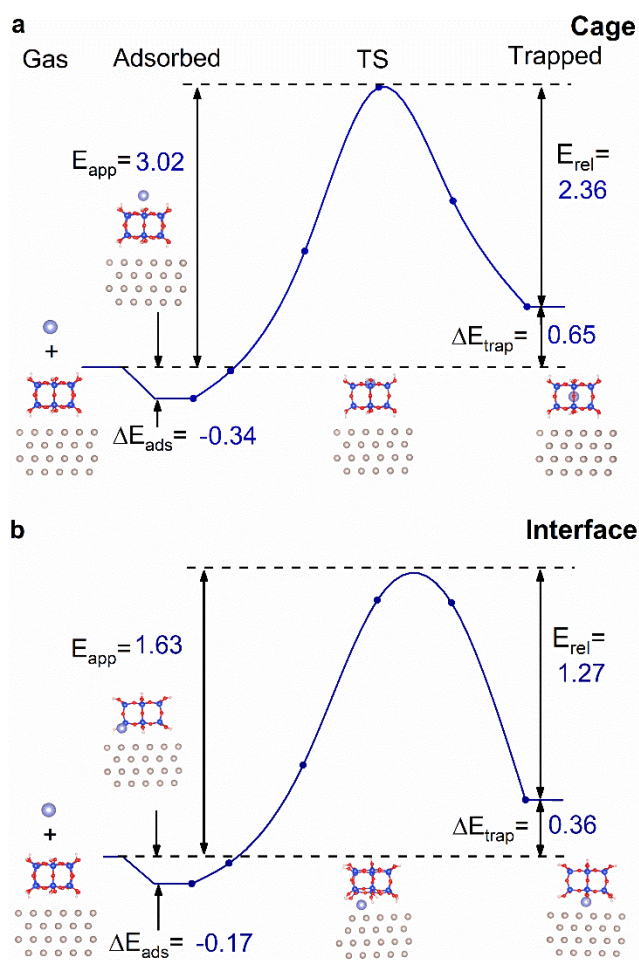


Figure 5. Xe trapping on silica nanocages supported on Ru: **(a)** Potential energy diagram for Xe trapping in a silica nanocage; **(b)** Potential energy diagram for Xe trapping at the interface of a silica nanocage and Ru surface. The minimum energy path for Xe trapping was calculated from the climbing image nudged elastic band method. Reaction coordinates can be found in Figure S14. Color code: Si (blue), O in silica films (red), H (light gray), Ru (silver), and Xe (purple). The effect of chemisorbed oxygen (0.25 of a monolayer) on Ru was investigated. Energy diagrams can be found in **Figure S16**. Chemisorbed oxygen destabilizes both adsorbed and trapped states by about 0.15 eV. Such an effect is translated into slightly lower release energies (2.18 eV in the presence of oxygen versus 2.36 eV in bare Ru). A lower release temperature occurs as a consequence of the reduced release energy barrier. Simulated TPD indicates 762 K for the O-covered surface and 813 K for the bare Ru surface, agreeing with the experimental TPD data (Figure S15).

Our experimental data also shows that the temperature enhances the formation of Si-O-Ru bonds, suggesting some anchoring of the cages. Another geometry was explored with DFT calculations as an extreme anchoring case to investigate this possibility: a nanocage with four anchoring

points (standing). Adsorption, trapping, and release energies were calculated for comparison and are presented in **Figure S17**. The trapping barrier was calculated to be 3.52 eV, 0.5 eV higher for the anchored cage than the flat one. Xe release, on the other hand, would be facilitated, with an E_{rel} of 1.99 eV. Other anchoring configurations of flat cages containing Si-O-Ru linkages were explored but always converged to the minimum energy system without Si-O-Ru linkages.

The experimental data in Figure S10 shows that upon heating, the binding energies of Si 2*p*, O 1*s*, and Xe 3*d* shift to higher values. The observation agrees with prior work for silica bilayers on Ru(0001), where removing chemisorbed oxygen by annealing results in shifts to higher binding energies.[24] Another contributing factor could be the formation of Si-O-Ru linkages. Our calculations on the 4-point anchored cage support this hypothesis. The Xe 3*d*_{5/2} peak position increases by 0.68 eV, while the peaks of Si 2*p* and O 1*s* attributed to silica cage shift equally by 0.3 eV. Simulated core-level energy shifts (Table S5) for the flat and anchored nanocages show about 0.58 eV for the Si 2*p* and 0.68 eV for the O 1*s* core levels. Calculated Xe 3*d* levels also show a shift of about 0.1 eV. Even though the calculated values overpredict (in the case of Si and O) or underpredict (in the case of Xe) the binding energy shifts, all of them indicate a positive shift, which is in qualitative agreement with experimental data trends.

The combined experimental and computational approaches used in this work show that silica nanocages in contact with a metal prepared with a scalable synthesis method are suitable for trapping Xe (and other noble gases). These results open opportunities for applications in various areas, including Xe containment in nuclear reactors, nuclear waste remediation, medical isotopes production, nuclear non-proliferation, noble gas capture, separation, and detection, and many others.

3. Conclusions

A nanostructure comprised of commercially available silica nanocages in contact with a metal support is used for irreversibly trapping Xe atoms. Xe enters the cages in the cationic form and gets neutralized by electron transfer from the metal, resulting in a trapped neutral species. This is confirmed by oxidation of the metal, which inhibits the trapping. The process is demonstrated in the temperature range between 400 and 600 K. Heating to 750 K is required to release the trapped Xe completely. A kinetic model for the trapping process is proposed and tested using kinetic Monte Carlo simulations, showing good agreement with experimental results. The optimum temperature range for Xe trapping is determined to be 500 ± 50 K. In conjunction with DFT calculations, experimental data suggest that the silica nanocages are rearranged and anchored to the Ru substrate through Ru-O-Si linkages at high temperatures.

This comprehensive work involved a new material synthesis approach that is potentially scalable, Xe gas trapping experiments using these materials, modeling the Xe trapping kinetics, and ab-initio calculations to understand the thermodynamics. This new material has a wide range of potential applications, including more efficient Xe production, safer and more efficient nuclear energy production, monitoring of non-proliferation of nuclear weapons, medical isotopes production, and others.

4. Methods

4.1. Ruthenium film preparation:

Ruthenium-coated sapphire wafers were prepared and used as supports to deposit silicate nanocages. A sapphire wafer was cleaned with soap water and rinsed with acetone and deionized

water. After that, 10 nm of chromium (Cr) was deposited by sputtering physical vapor deposition (PVD), followed by the deposition of ~20 nm of Ru using the same method. X-ray photoelectron spectroscopy (XPS) was used to confirm the presence of Ru and the absence of Al and Cr in the near-surface region.

4.2. Silica nanocage deposition:

The source material for the silica nanocages, Dodecaphenyl-POSS (D-POSS), was purchased from Sigma-Aldrich (Dodecaphenyl-POSS, CAS Number 18923-59-6, Sigma-Aldrich, MQ100). A KN 2002 KSV NIMA Langmuir trough was used for the deposition. The trough top inner dimensions are 364×75 mm.

15 mg of D-POSS were first dissolved in 5 mL toluene. Deionized (DI) water was used for filling the trough. Four drops of prepared solution (~200 μ L) were dropped and spread on the DI water in the trough. After three hours (to guarantee toluene evaporation), the Ru film was immersed in the solution in the trough such that the sample plane was orthogonal to the trough plane. The setup barriers were adjusted to reach a surface tension of 20 mN/m, which is the first derivative turning point of surface tension isotherm expected to correspond to one monolayer[33] (see Figure S2). The substrate was pulled out at a rate of 0.5 mm/min while the surface tension was kept constant at 20 mN/m. After deposition, the film was calcined in a muffle furnace in air at a temperature of 500 °C with a rate of 10 °C/min and kept for 30 min to remove the phenyl groups on deposited molecules.

4.3. Materials characterization

XPS experiments in Figure S1 were performed using a system equipped with a SPECS PHOIBOS NAP 150 hemispherical analyzer and a monochromatic Al K α X-ray source. The spectra were acquired under UHV conditions (base pressure of 2×10^{-9} mbar) and 298 K. The spectra were acquired on sample areas smaller than $300 \mu\text{m} \times 300 \mu\text{m}$.

AFM images were obtained on Park NX20 microscope with non-contact mode.

IRRAS experiments were performed in a Bruker Vertex 80V spectrometer from which infrared light is directed into a UHV analysis chamber to interact with the sample surface at a grazing incidence ($\sim 8^\circ$). In this work, the s-polarized spectrum was collected as background and subtracted from the p-polarized spectrum for all experiments to eliminate gas-phase contributions. A liquid-nitrogen-cooled mercury–cadmium–telluride (MCT) detector was used. Spectra were collected using a resolution of 4 cm^{-1} and 1000 scans.

Raman spectroscopy experiments were performed on a WiTEC alpha300 microscope with a 532 nm laser. The spectra were taken with 100X scope magnification, 20 mW laser power. Each scan took 20 s, and ten scans were taken for each sample.

4.4. Xenon trapping experiment:

Xenon trapping experiments were performed at an ambient pressure XPS instrument (AP-XPS) at the 23-ID-2 beamline (IOS) of the National Synchrotron Light Source II (NSLS-II). The photon energy of 983 eV was used unless specified otherwise. The main chamber (base pressure 2×10^{-9} Torr) of the end-station was equipped with a differentially pumped hemispherical analyzer (Specs Phoibos 150 NAP), which was offset by 70° from the incident synchrotron X-ray beam. Gases, including Xe, were introduced to the main chamber through precision variable

leak valves. The Ru $3d_{5/2}$ core level binding energy is fixed at 280.0 eV for energy calibration purposes.

During trapping experiments, the stage was heated to a set temperature. The sample was then exposed to 1 Torr of Xe in the presence of X-rays while taking XP spectra every 10 min.

Trapping experiments were carried out at 1 Torr of Xe at 420, 480, or 600 K, and the coverage was followed as a function of time. After 70 min, the chamber was evacuated, and the sample was heated 900 K in vacuum for 10 min to remove the trapped Xe.

Release experiments were conducted after trapping at 420 K (1 Torr of Xe for 20 min). Gas-phase Xe was removed, and the stage was flashed to a target temperature (and cooled back to 420 K) until no Xe $3d$ peak was observed. All the measurements were done at 420 K. The maximum temperature applied was 850 K.

4.5. Computational details:

All calculations were performed using the plane-wave-based DFT method in the Vienna Ab initio simulation package (VASP) [34]. The electron-ion interaction was described using the projector augmented wave (PAW) method [35]. The generalized gradient approximation and the Perdew-Burke-Ernzerhof functional (GGA-PBE) were used to describe the type of exchange-correlation [36]. Van der Waals dispersions were applied by the dDsC dispersion correction method (DFT-dDsC) [37]. A dipole correction was also included in the z-direction of the supercell. Ru(0001) substrate was modeled using four layers of Ru atoms with and without O atoms with a 0.2 ML coverage. The system consists of a hexagonal SiO₂ cage terminated by -OH groups. Two configurations were optimized to probe anchoring of the cages to the substrate: a flat cage with hexagonal aperture parallel to the substrate (similar to the SiO₂ bilayers) or a

standing cage with four anchoring points, making Si-O-Ru bonds (Figure S13). The supercell has 13.6 Å x 13.6 Å x 45.4 Å. A kinetic energy cutoff of 400 eV was used, and the Monkhorst-Pack sampled the Brillouin zone with 2x2x1 points. The bottom two Ru layers were held fixed. All the other atoms were allowed to relax until the energy difference, and the forces were smaller than 1x10⁻⁶ eV and 0.05 eV/ Å, respectively.

The core-level binding energies (BE) were calculated using the Slater-Janak transition state approach for Xe.[38, 39] All BE values of Xe 3d were given relative to the BE of trapped atoms in the flat cage (Table S5 in the Supporting Information).

Temperature-programmed desorption was simulated by assuming a first-order reaction law $I = I_0 \exp(-kt)$, where I_0 is the initial relative amount of trapped Xe (first XPS data point at 420 K).

The release rate constants (k) were evaluated based on the Arrhenius equation $k = A \exp(-E_{rel}/(k_B T))$ [40], where k_B is the Boltzmann constant and T is the temperature. The release energy E_{rel} is obtained from DFT by using the climbing image nudged elastic band method (CI-NEB) [32] implemented in VASP. The pre-exponential factor A is calculated based on the transition state theory considering gas permeation over a pore aperture [41], $A =$

$$\frac{1}{L} \sqrt{\frac{k_B T}{2\pi m}} \exp\left(\frac{\Delta S}{k_B}\right),$$

where L is the thickness of the bilayer after the trapping of atoms and m is the

mass of the Xe atom. ΔS is the entropy difference of the initial (S_i , initial meaning trapped in this case) and the transition state (S_{TS}). The entropy is calculated as $S = k_B \sum_i^{modes} \left(\frac{x_i}{e^{x_i} - 1} - \ln(1 - e^{-x_i}) \right)$, where x_i for each vibrational mode is defined in the vibrational frequency, ν_i , as $x_i =$

$$\frac{h\nu_i}{k_B T}.$$

[42] The vibrational frequencies were calculated by the finite displacement method as

implemented in VASP. During the calculations of the vibrational frequencies, the positions of the bilayer and Ru substrate are kept fixed.

Supporting Information

Supporting information is available from the Wiley Online Library or the authors.

Acknowledgments

The research was performed at the Center for Functional Nanomaterials and the 23-ID-2 (IOS) beamline of the National Synchrotron Light Source II, Brookhaven National Laboratory, supported by the U.S. Department of Energy, Office of Basic Energy Sciences, under Contract No. DE-SC0012704. Z.D. is supported by ACS PRF grant # 61059-ND5. The computational part of this work was supported by the Catalysis Center for Energy Innovation, an Energy Frontier Research Center funded by the U.S. Department of Energy, Office of Science, Office of Basic Energy Sciences under Award No. DE-SC0001004.

Received: ((will be filled in by the editorial staff))

Revised: ((will be filled in by the editorial staff))

Published online: ((will be filled in by the editorial staff))

Conflict of interest

The authors declare no conflict of interest.

References:

1. Bondarenko, V. L.; Kupriyanov, M. Y.; Ustyugova, T. G.; Verkhovnyi, A. I.; Stefanovskii, A. N., *Chemical and Petroleum Engineering* **2019**, *54* (11-12), 806-814. DOI 10.1007/s10556-019-00554-4.
2. Anderson, P. D. J. J. T. D. J. M. High efficacy electrodeless high intensity discharge lamp. 4810938, **1989**.
3. Kireev, S. G.; Kulebiakina, A. I.; Shashkovskiy, S. G., *Journal of Applied Spectroscopy* **2019**, *86* (4), 685-689. DOI 10.1007/s10812-019-00879-1.
4. L. C. David, J. T. V. a. S. R. N. A. S., Ion Propulsion Technology: NASA's Evolutionary Xenon Thruster (NEXT) Development and Long Duration Tests Results and its Applications. In *2020 Advances in Science and Engineering Technology International Conferences*, Dubai, United Arab Emirates, **2020**; pp 1-5.
5. Preckel, B.; Weber, N. C.; Sanders, R. D.; Maze, M.; Schlack, W., *Anesthesiology* **2006**, *105* (1), 187-97. DOI 10.1097/00000542-200607000-00029.
6. Abramov, I. S.; Gospodchikov, E. D.; Shalashov, A. G., *Physical Review Applied* **2018**, *10* (3). DOI 10.1103/PhysRevApplied.10.034065.
7. Neice, A. E.; Zornow, M. H., *Anaesthesia* **2016**, *71* (11), 1267-1272. DOI 10.1111/anae.13569.
8. Shcheka, S. S.; Keppler, H., *Nature* **2012**, *490* (7421), 531-4. DOI 10.1038/nature11506.
9. Mercier, B.; Yang, D.; Zhuang, Z.; Liang, J., *EPJ Nuclear Sciences & Technologies* **2021**, *7*. DOI 10.1051/epjn/2020021.
10. Bowyer, T. W.; Schlosser, C.; Abel, K. H.; Auer, M.; Hayes, J. C.; Heimbigner, T. R.; McIntyre, J. I.; Panisko, M. E.; Reeder, P. L.; Satorius, H.; Schulze, J.; Weiss, W., *J Environ Radioact* **2002**, *59* (2), 139-51. DOI 10.1016/s0265-931x(01)00042-x.

11. Bazan, R. E.; Bastos-Neto, M.; Moeller, A.; Dreisbach, F.; Staudt, R., *Adsorption* **2011**, *17* (2), 371-383. DOI 10.1007/s10450-011-9337-3.
12. Xiong, S. S.; Liu, Q.; Wang, Q.; Li, W.; Tang, Y. M.; Wang, X. L.; Hu, S.; Chen, B. L., *J Mater Chem A* **2015**, *3* (20), 10747-10752. DOI 10.1039/c5ta00460h.
13. Banerjee, D.; Simon, C. M.; Elsaidi, S. K.; Haranczyk, M.; Thallapally, P. K., *Chem* **2018**, *4* (3), 466-494. DOI 10.1016/j.chempr.2017.12.025.
14. Papadopoulos, R. M. B. F. R. S. R., *Proceedings of the Royal Society of London. A. Mathematical and Physical Sciences* **1997**, *326* (1566), 315-330. DOI 10.1098/rspa.1972.0011.
15. Daniel, C.; Elbaraoui, A.; Aguado, S.; Springuel-Huet, M.-A.; Nossov, A.; Fontaine, J.-P.; Topin, S.; Taffary, T.; Deliere, L.; Schuurman, Y.; Farrusseng, D., *The Journal of Physical Chemistry C* **2013**, *117* (29), 15122-15129. DOI 10.1021/jp403934r.
16. Kuznicki, S. M.; Ansón, A.; Koenig, A.; Kuznicki, T. M.; Hastrup, T.; Eyring, E. M.; Hunter, D., *The Journal of Physical Chemistry C* **2007**, *111* (4), 1560-1562. DOI 10.1021/jp067630t.
17. BARRETT, P., A.; STEPHENSON, Neil, A.; STUCKERT, Nicholas, R.; FREIERT, Michael; DU, Hai; MASIN, Rachael, A.; SWINDLEHURST, Garrett, R. Cryogenic adsorption process for xenon recovery. **2018**.
18. Zhong, J. Q.; Wang, M.; Akter, N.; Kestell, J. D.; Boscoboinik, A. M.; Kim, T.; Stacchiola, D. J.; Lu, D.; Boscoboinik, J. A., *Nat Commun* **2017**, *8*, 16118. DOI 10.1038/ncomms16118.
19. Zhong, J. Q.; Wang, M.; Akter, N.; Kestell, J. D.; Niu, T.; Boscoboinik, A. M.; Kim, T.; Stacchiola, D. J.; Wu, Q.; Lu, D.; Boscoboinik, J. A., *Advanced Functional Materials* **2019**, *29* (20). DOI 10.1002/adfm.201806583.
20. Loffler, D.; Uhlrich, J. J.; Baron, M.; Yang, B.; Yu, X.; Lichtenstein, L.; Heinke, L.; Buchner, C.; Heyde, M.; Shaikhutdinov, S.; Freund, H. J.; Włodarczyk, R.; Sierka, M.; Sauer, J., *Phys Rev Lett* **2010**, *105* (14), 146104. DOI 10.1103/PhysRevLett.105.146104.
21. J. Boscoboinik, N. A., A. Boscoboinik, M. Wang, Y. Xu, J. Zhong, D. Lu, D. Stacchiola. Oxide Polygonal Prism Nanocages for Trapping of Gases.
22. Inc, H. P. <https://hybridplastics.com>.
23. Morgan, D. J., *Surface and Interface Analysis* **2015**, *47* (11), 1072-1079. DOI 10.1002/sia.5852.
24. Wang, M. G.; Zhong, J. Q.; Kestell, J.; Waluyo, I.; Stacchiola, D. J.; Boscoboinik, J. A.; Lu, D. Y., *Top Catal* **2017**, *60* (6-7), 481-491. DOI 10.1007/s11244-016-0704-x.
25. Kremer, G.; Alvarez Quiceno, J. C.; Lisi, S.; Pierron, T.; Gonzalez, C.; Sicot, M.; Kierren, B.; Malterre, D.; Rault, J. E.; Le Fevre, P.; Bertran, F.; Dappe, Y. J.; Coraux, J.; Pochet, P.; Fagot-Revurat, Y., *ACS Nano* **2019**, *13* (4), 4720-4730. DOI 10.1021/acsnano.9b01028.
26. Shchukarev, A.; Rosenqvist, J.; Sjöberg, S., *Journal of Electron Spectroscopy and Related Phenomena* **2004**, *137-140*, 171-176. DOI 10.1016/j.elspec.2004.02.095.
27. Papparazzo, E.; Fanfoni, M.; Severini, E.; Priori, S., *Journal of Vacuum Science & Technology A: Vacuum, Surfaces, and Films* **1992**, *10* (4), 2892-2896. DOI 10.1116/1.577726.
28. Bulnes, F. M.; Pereyra, V. D.; Riccardo, J. L., *Phys Rev E* **1998**, *58* (1), 86-92. DOI DOI 10.1103/PhysRevE.58.86.
29. Marro, J.; Bortz, A. B.; Kalos, M. H.; Lebowitz, J. L., *Physical Review B* **1975**, *12* (6), 2000-2011. DOI 10.1103/PhysRevB.12.2000.
30. Sales, J. L.; Unac, R. O.; Gargiulo, M. V.; Bustos, V.; Zgrablich, G., *Langmuir* **1996**, *12* (1), 95-100. DOI DOI 10.1021/la940859s.
31. Sadiq, A., *J Comput Phys* **1984**, *55* (3), 387-396. DOI Doi 10.1016/0021-9991(84)90028-7.
32. Henkelman, G.; Uberuaga, B. P.; Jónsson, H., *The Journal of Chemical Physics* **2000**, *113* (22), 9901-9904. DOI 10.1063/1.1329672.
33. Ahmed, I.; Dildar, L.; Haque, A.; Patra, P.; Mukhopadhyay, M.; Hazra, S.; Kulkarni, M.; Thomas, S.; Plaisier, J. R.; Dutta, S. B.; Bal, J. K., *J Colloid Interface Sci* **2018**, *514*, 433-442. DOI 10.1016/j.jcis.2017.12.037.

34. Kresse, G.; Furthmüller, J., *Phys Rev B Condens Matter* **1996**, *54* (16), 11169-11186. DOI 10.1103/physrevb.54.11169.
35. Blochl, P. E., *Phys Rev B Condens Matter* **1994**, *50* (24), 17953-17979. DOI 10.1103/physrevb.50.17953.
36. Perdew, J. P.; Burke, K.; Ernzerhof, M., *Phys Rev Lett* **1996**, *77* (18), 3865-3868. DOI 10.1103/PhysRevLett.77.3865.
37. Steinmann, S. N.; Corminboeuf, C., *J Chem Phys* **2011**, *134* (4), 044117. DOI 10.1063/1.3545985.
38. Lizzit, S.; Baraldi, A.; Groso, A.; Reuter, K.; Ganduglia-Pirovano, M. V.; Stampfl, C.; Scheffler, M.; Stihler, M.; Keller, C.; Wurth, W.; Menzel, D., *Physical Review B* **2001**, *63* (20). DOI 10.1103/PhysRevB.63.205419.
39. Köhler, L.; Kresse, G., *Physical Review B* **2004**, *70* (16). DOI 10.1103/PhysRevB.70.165405.
40. Campbell, C. T.; Árnadóttir, L.; Sellers, J. R. V., *Zeitschrift für Physikalische Chemie* **2013**, *227* (9-11). DOI 10.1524/zpch.2013.0395.
41. Yuan, Z.; Govind Rajan, A.; Misra, R. P.; Draushuk, L. W.; Agrawal, K. V.; Strano, M. S.; Blankschtein, D., *ACS Nano* **2017**, *11* (8), 7974-7987. DOI 10.1021/acsnano.7b02523.
42. Gokhale, A. A.; Kandoi, S.; Greeley, J. P.; Mavrikakis, M.; Dumesic, J. A., *Chemical Engineering Science* **2004**, *59* (22-23), 4679-4691. DOI 10.1016/j.ces.2004.09.038.
43. Handke, B.; Klita, Ł.; Nizioł, J.; Jastrzębski, W.; Adamczyk, A., *Journal of Molecular Structure* **2014**, *1065-1066*, 248-253. DOI 10.1016/j.molstruc.2014.02.053.
44. Jalarvo, N.; Gourdon, O.; Ehlers, G.; Tyagi, M.; Kumar, S. K.; Dobbs, K. D.; Smalley, R. J.; Guise, W. E.; Ramirez-Cuesta, A.; Wildgruber, C.; Crawford, M. K., *J Phys Chem C* **2014**, *118* (10), 5579-5592. DOI 10.1021/jp412228r.
45. Adar, F., *Spectroscopy* **2016**, *31* (7), 16-23.
46. Martinelli, A.; Creci, S.; Vavra, S.; Carlsson, P. A.; Skoglundh, M., *Phys Chem Chem Phys* **2020**, *22* (3), 1640-1654. DOI 10.1039/c9cp06199a.

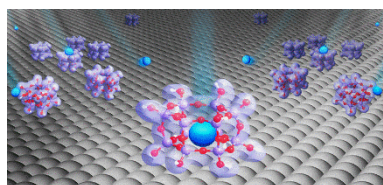
Table of contents:

In this work, we produce a material using silica nanocages supported on a thin ruthenium film to explore its behavior toward Xe trapping. We use synchrotron-based ambient pressure X-ray photoelectron spectroscopy (AP-XPS) to follow the Xe trapping, exploring mechanistic aspects of this process by combining experimental, theoretical, and simulation tools.

Y. Xu, M. Dorneles de Mello C. Zhou, S. Sharma, B. Karagoz, A. Head, Z. Darbari, I. Waluyo, A. Hunt, D. J. Stacchiola, S. Manzi, A. M. Boscoboinik, V. D. Pereyra and J. Anibal Boscoboinik**

Xenon Trapping in Metal-Supported Silica Nanocages

ToC figure



Supporting Information

Xenon Trapping in Metal-Supported Silica Nanocages

Yixin Xu, Matheus Dorneles de Mello Chen Zhou, Shruti Sharma, Burcu Karagoz, Ashley Head, Zubin Darbari, Iradwikanari Waluyo, Adrian Hunt, Dario J. Stacchiola, Sergio Manzi, Alejandro M. Boscoboinik, Victor D. Pereyra and J. Anibal Boscoboinik**

Section S1: Silica nanocage deposition and characterization

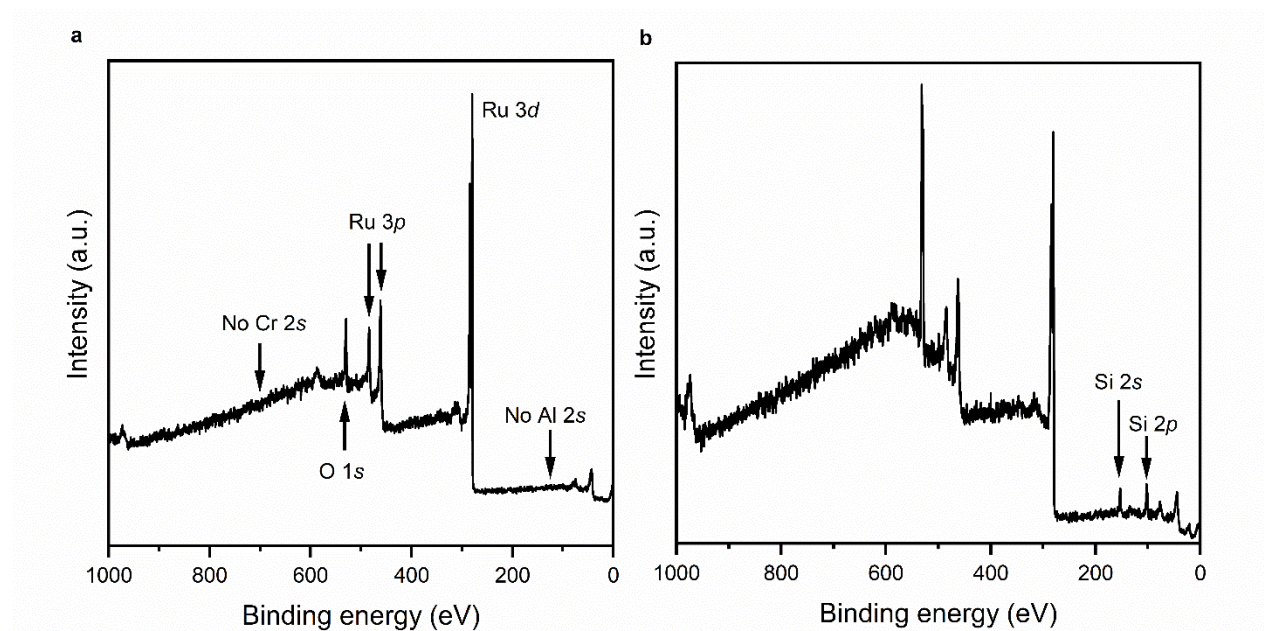


Figure S1. Survey XPS of (a) Ru film and (b) D-POSS molecules on Ru film.

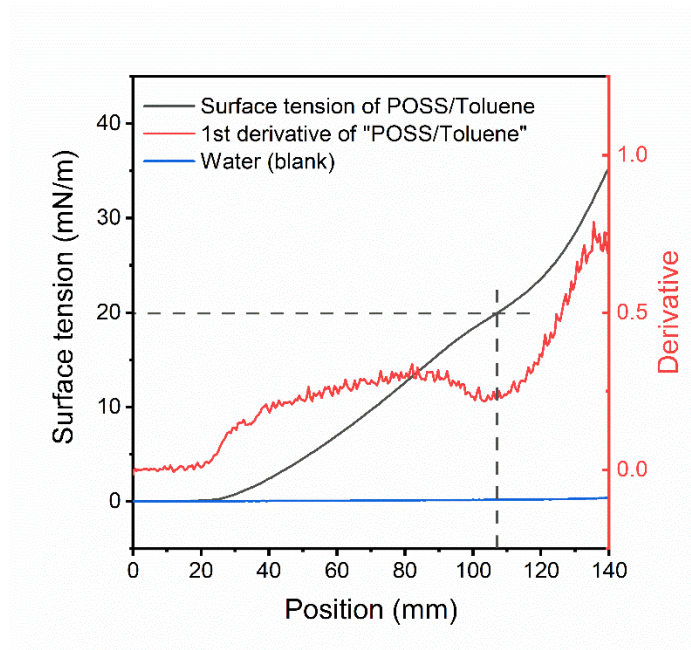


Figure S2. Langmuir trough deposition of D-POSS cages: surface tension and its first derivative versus position of trough barriers.

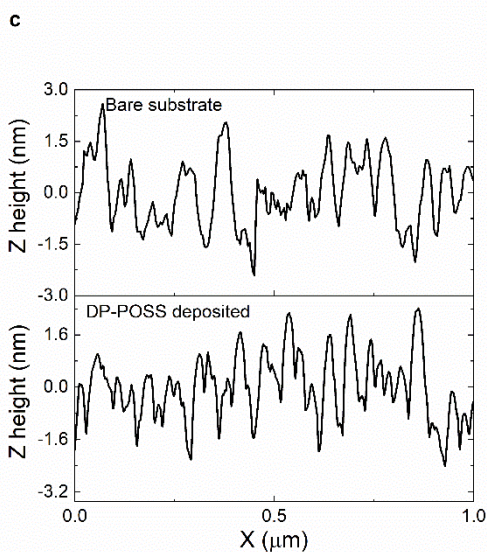
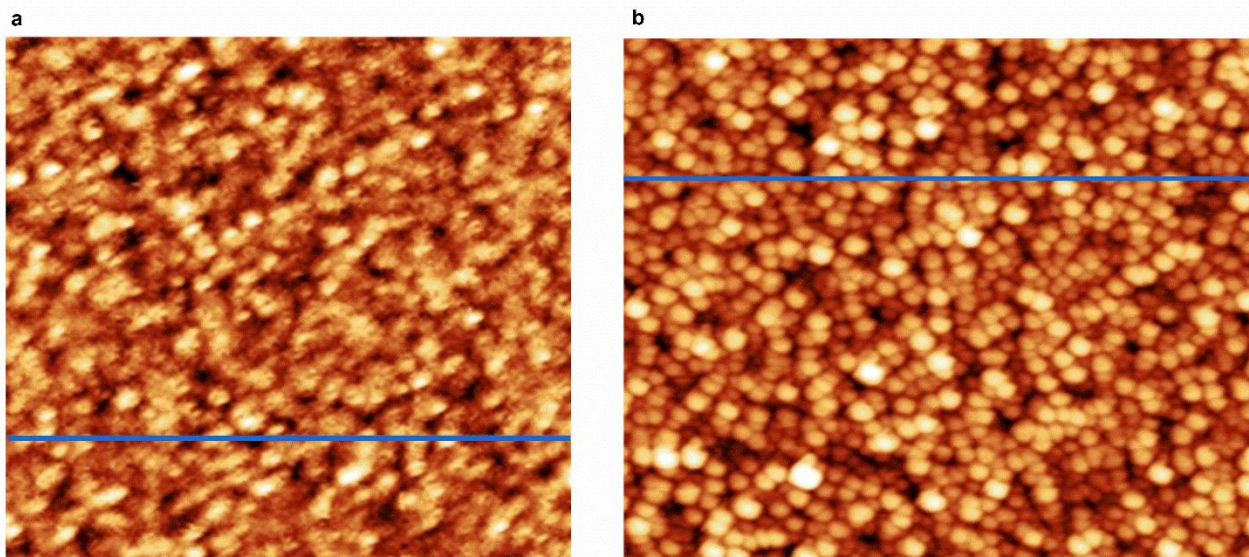


Figure S3. AFM images of (a) bare Ru film on sapphire; (b) D-POSS molecules Ru film; (c) line profiles in parts (a) and (b).

Figure S3 shows the AFM results for the surface before and after D-POSS deposition.

Comparing line profiles (Figure S3c) before and after D-POSS deposition, they both have height variations in the -3 nm to 3 nm range. There are no apparent morphology changes upon D-POSS deposition.

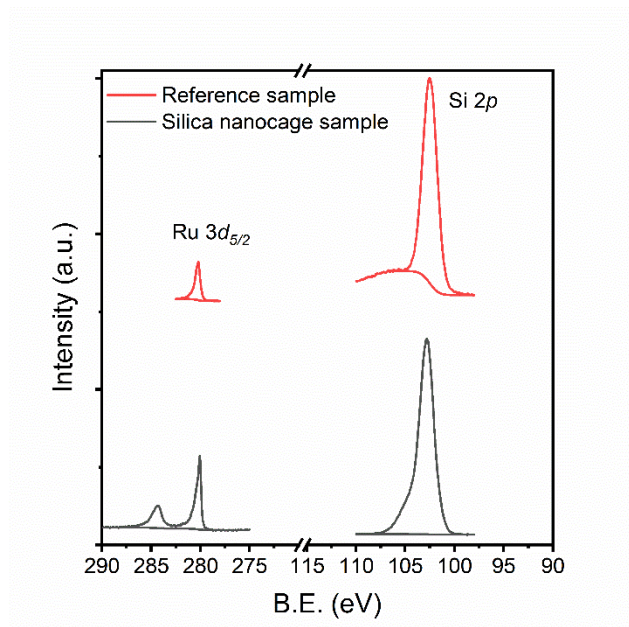


Figure S4. XPS of D-POSS/Ru sample (black) and a bilayer Al_{0.25}Si_{0.75}O₂/Ru (red). The Al_{0.25}Si_{0.75}O₂/Ru sample has a known Si coverage and is used here as a reference to estimate the coverage of the D-POSS/Ru sample.

The ratio between the Si 2p and Ru 3d_{5/2} peaks for each sample shown in Figure S4 is used to estimate a silicate coverage (nanocages) of 42%. The area ratios are shown in Table S1.

Table S1. Silicon quantification on silica nanocages

	Si 2p / Ru 3d _{5/2}	Si coverage
Silica nanocage	7.28	42%
Reference (Aluminosilicate bilayer film)	13.09	75%

Vibrational Spectroscopy

Infrared reflection absorption spectroscopy (IRRAS) of the deposited film before calcination (black curve in **Figure S5a**) shows vibrations at 2925 cm⁻¹, characteristic of C-H bonds. We also observe a peak at 1130 cm⁻¹, indicative of Si-O-Si regions.[43] The peak intensity at 2925 cm⁻¹

becomes significantly reduced upon calcination (red curve in Figure S5a). The Si-O-Si peak shifts towards 1238 cm^{-1} that is possibly attributed to oligomerization of the cages. The absence of a peak at $\sim 1300\text{ cm}^{-1}$, characteristic of bilayer silicates, indicates that a more disordered arrangement of cages is formed.[20] We further characterized the films by Raman spectroscopy (**Figure S5b** and **Figure S5c**). The deposited film containing a sub-monolayer of silica nanocages showed a weak Raman signal given the low coverage, so significant features could be assessed. To obtain a better signal and understand the role of calcination, we prepared a new set of samples by drop-casting the POSS molecules ($5\text{ }\mu\text{mol}$) on a Ru-coated sapphire substrate. Raman shift peaks at 1001 cm^{-1} and 1031 cm^{-1} are assigned to aromatic ring breathing. Peaks at 750 cm^{-1} , 855 cm^{-1} , 920 cm^{-1} , 1596 cm^{-1} , and 3057 cm^{-1} are assigned to C-H. The other peaks at 396 cm^{-1} , 622 cm^{-1} and 1137 cm^{-1} could be assigned to Si-O-Si bonds.[44-46] The data shows that upon calcination the peaks related to Si-O bonds remain intact, indicating that the silica cage structure is preserved. Moreover, a new peak at 1290 cm^{-1} appears after the calcination, suggesting some degree of oligomerization of the cages to form an extended network, similar to the observation for the thin films by IRRAS.

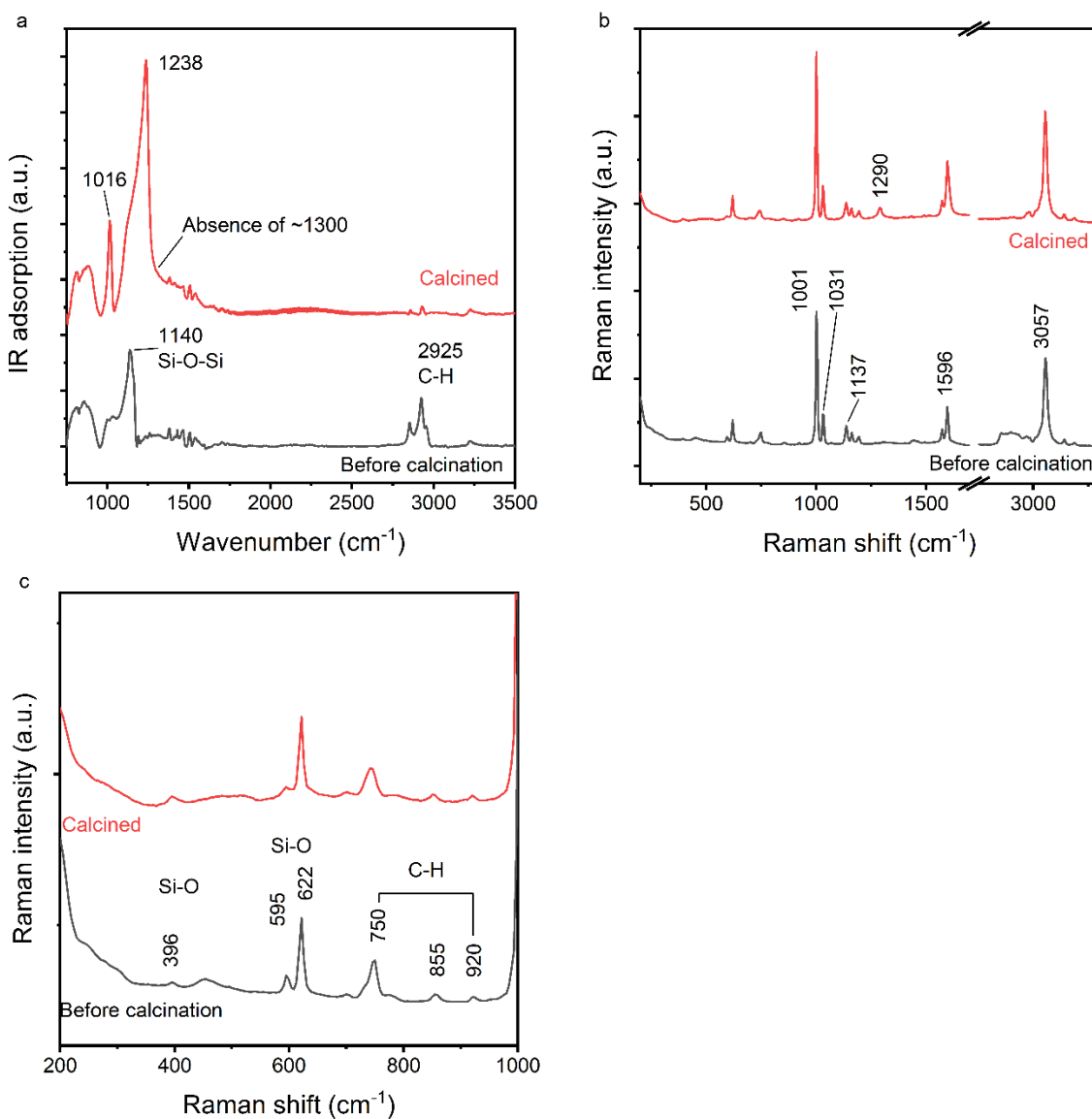


Figure S5. (a) IRRAS of D-POSS molecules on Ru deposited using a Langmuir trough before (black) and after (curve) calcination. (b) Raman spectra of D-POSS molecules deposited by drop-casting before (black) and after (red) calcination. (c) Expanded view of the low-energy region of the Raman spectrum. The drop-casted films were prepared to purposely have a much larger coverage of D-POSS cages to obtain a reasonable Raman signal. However, only the low-coverage films deposited using the Langmuir trough were used for all the trapping experiments described in the manuscript.

Section S2: Xe trapping on D-POSS/Ru

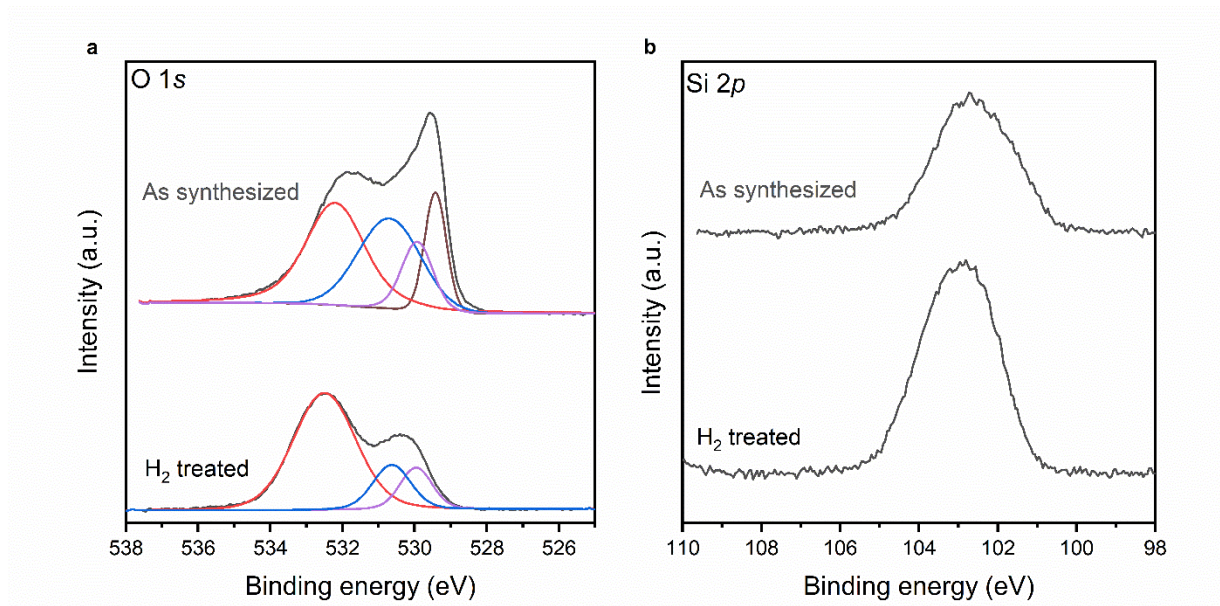


Figure S6. XPS spectra of the as-synthesized film (after calcination) and after H₂ treatment: (a) O 1s fittings: Si-O-Si (red), Ru-O-Si (blue), chemisorbed O on Ru (purple), and Ru-O (brown); (b) Si 2p region.

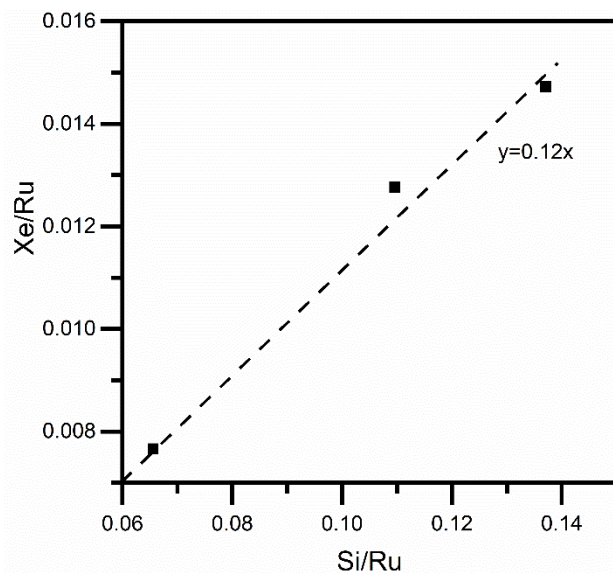


Figure S7. Correlation between Si_{2p}/Ru_{3d} ratios and Xe_{3d}/Ru_{3d} uptake at different spots in the specimen. Uptake at 420 K after dosing 1 Torr Xe for 70 min.

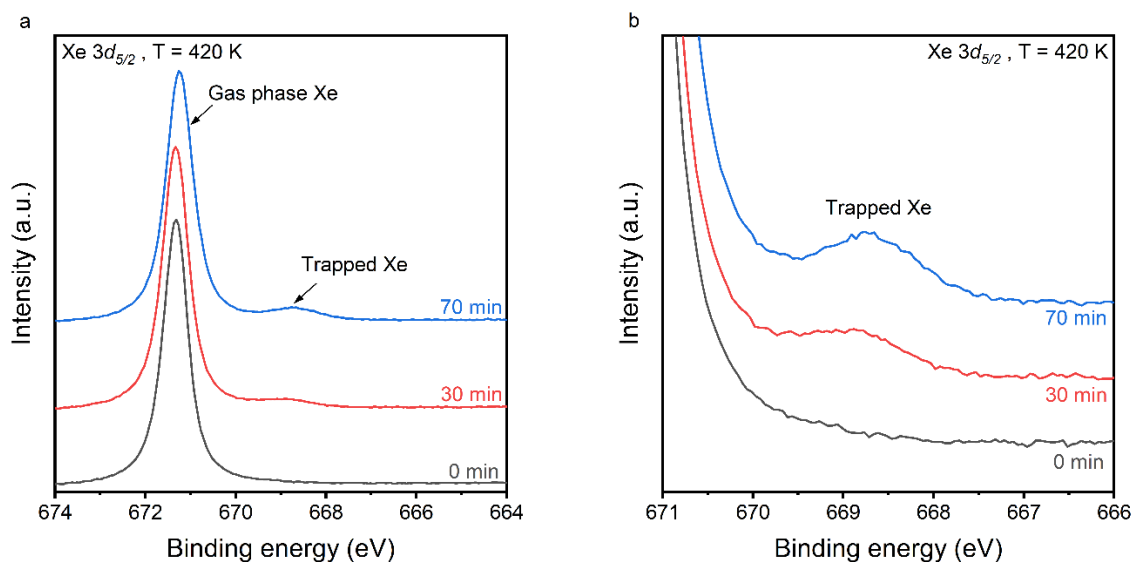


Figure S8. XPS of Xe 3d_{5/2} region at 420 K and different Xe exposure ($P_{Xe}=1$ Torr). Representative spectra at 0 min (black), 30 min (red), and 70 min (blue) highlight the difference in binding energies of Xe in the gas phase and Xe in the cages.

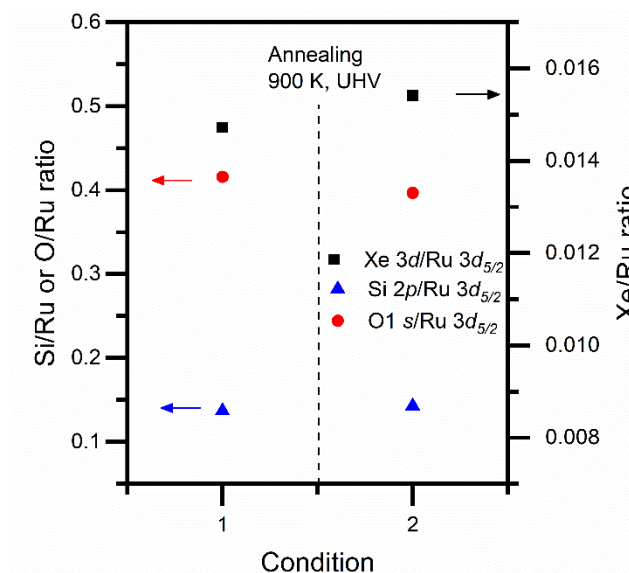


Figure S9. Peak area ratios of trapped Xe, O, and Si of nanocages after Xe is saturated at different conditions: (1) 420 K, and (2) 480 K. After each condition, the sample is annealed at 900 K under UHV for 10 min to guarantee Xe removal.

Table S2. Initial Xe trapping rates and O 1s / Ru 3d_{5/2} peak area ratios of all O components at different temperatures.

Temperature (K)	Trapping rate (min ⁻¹)	OH	Si-O-Si	Ru-O-Si	Chem. O
420	0.018	0.20	0.43	0.05	0.06
480	0.028	0.16	0.43	0.05	0.08
600	0.005	0.14	0.40	0.10	0.10

As discussed in the paper, the increase in the coverage of Xe is linearly proportional to time during the first 30 minutes. The Xe coverage saturates in 70 min at 420 K, and the [Xe 3d_{5/2} / Ru 3d_{5/2}] area ratio at this point is used as a reference to normalize the maximum coverage to 1. Based on the fittings of the normalized peak area ratio, the initial trapping rates are calculated and shown in Table S2. The peak area ratios of O components are calculated by dividing the raw peak area of the O 1s component by the raw peak area of Ru 3d_{5/2}.

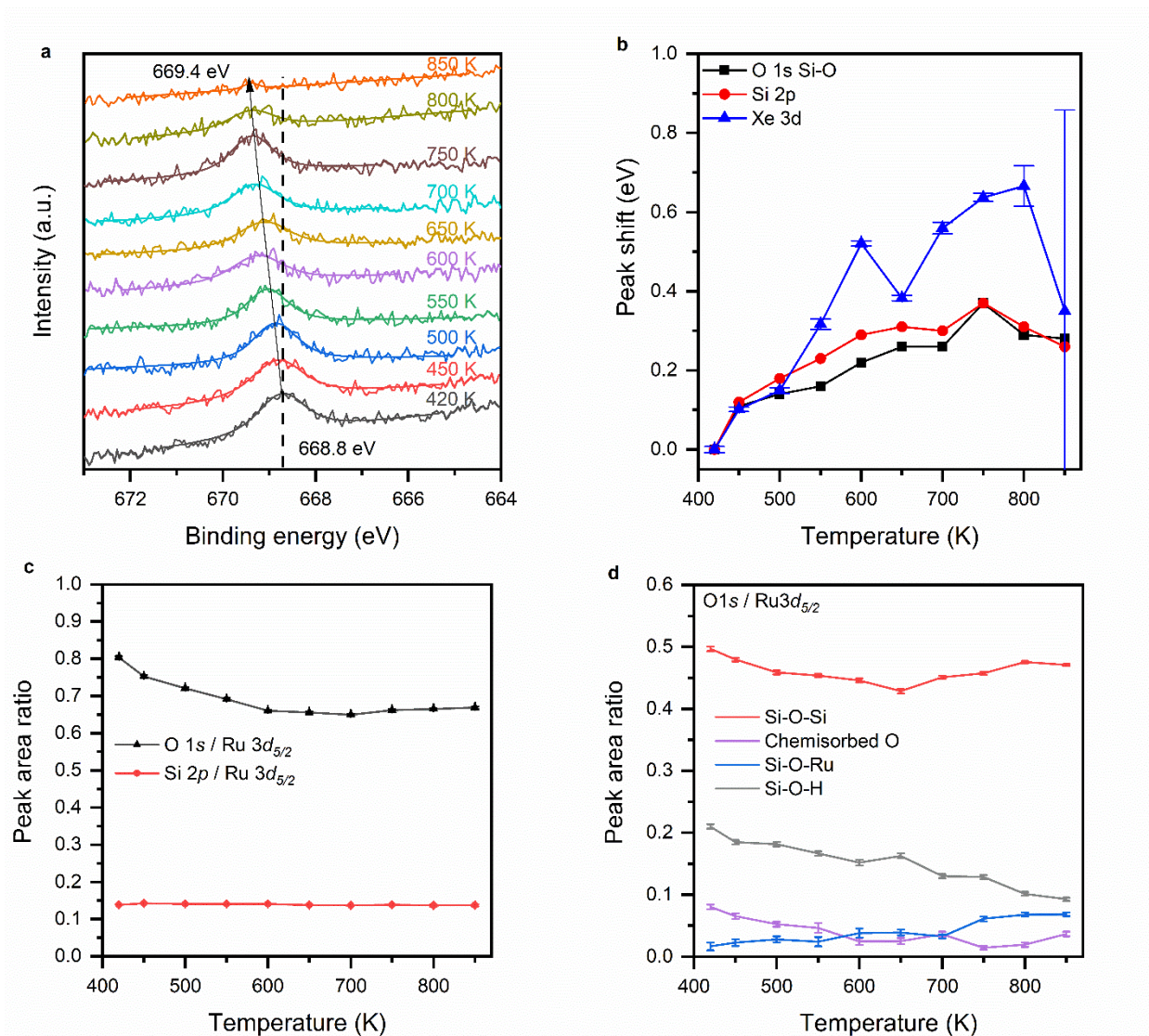


Figure S10. (a) Xe 3d_{5/2} XPS region during temperature programmed release experiment. Trapping was carried out at 420 K; (b) Binding energy shifts for Xe 3d, Si 2p, and O 1s. Both oxygen and silicon curves are associated with the ones assigned to the nanocages; (c) Peak area ratio of O 1s / Ru 3d_{5/2} and Si 2p / Ru 3d_{5/2} after heating to different temperatures; (d) O 1s speciation after heating to different temperatures (areas divided by Ru 3d_{5/2}).

Section S3: Kinetic Monte Carlo and Molecular Dynamics data

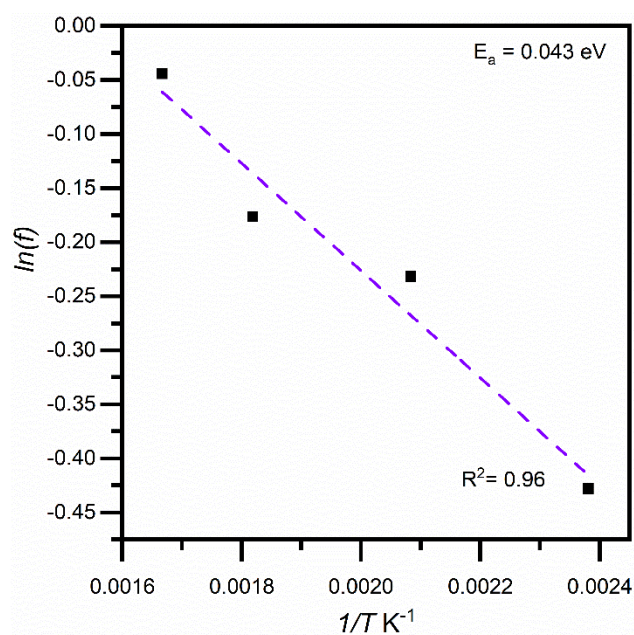
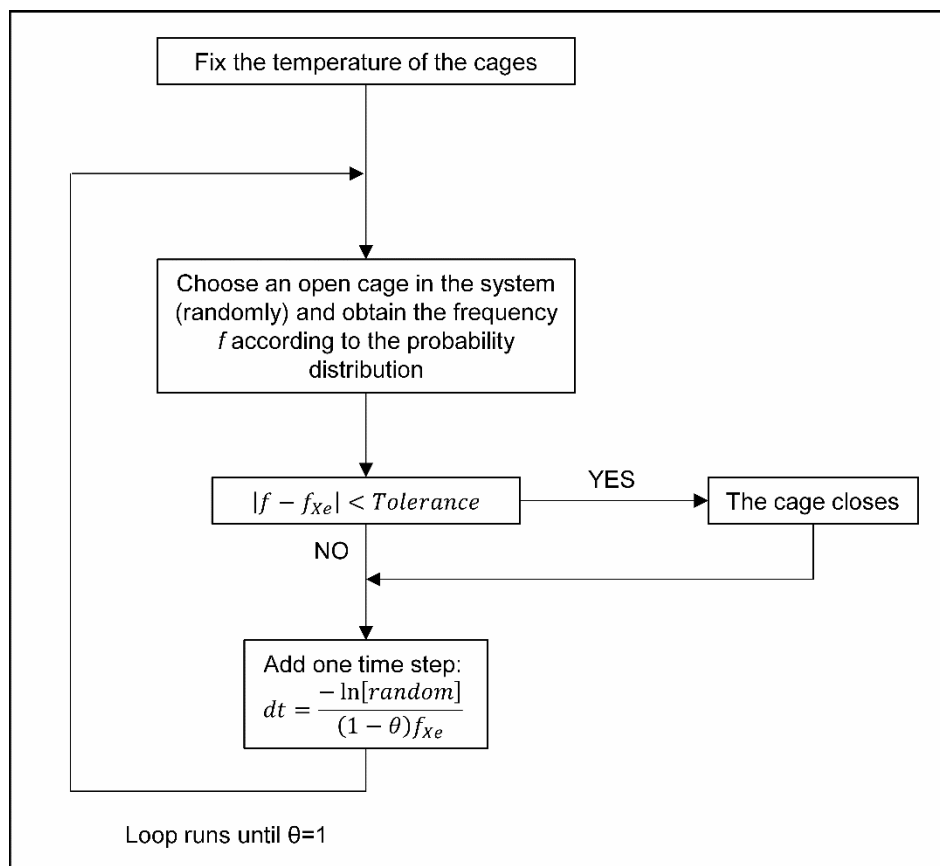


Figure S11. $\ln(f)$ vs. $1/T$ plot obtained from the MD simulations on the nanocages vibrating at different temperatures.



Scheme S1. Monte Carlo algorithm used to simulate Xe trapping in the nanocages.

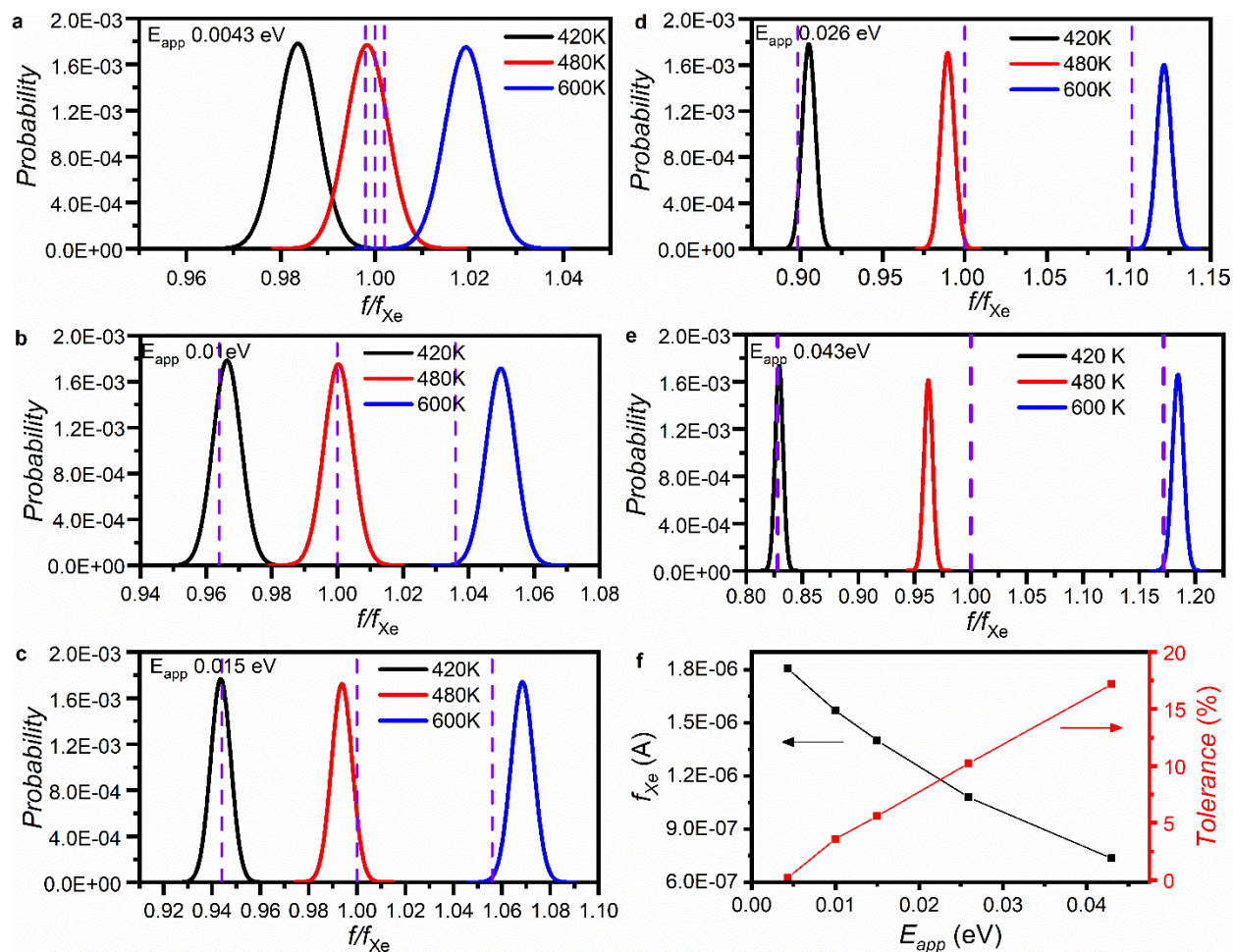


Figure S12. Probability density of a cage opening at similar frequency in which a Xe cation attempts to enter the cage considering different activation energies: (a) $E_{app} = 0.0043$ eV; (b) $E_{app} = 0.01$ eV; (c) $E_{app} = 0.015$ eV; (d) $E_{app} = 0.026$ eV; (e) $E_{app} = 0.043$ eV; the violet dashed line indicates the tolerance parameter used. (f) Estimated Xe frequencies at different activation energies and the tolerance parameters required to accept the occurrence of a trapping event.

Section S4: Density functional theory calculations

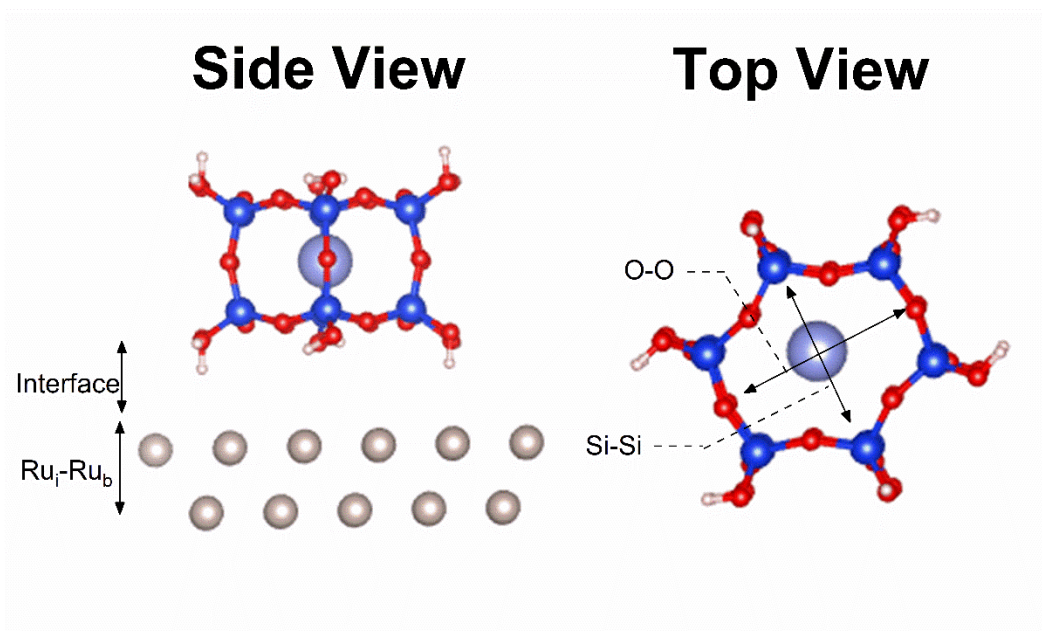


Figure S13. Schematic of silica nano-cage indicating parameters used to track expected changes upon Xe trapping in the nanocage: (i) distance between Ru atoms at the interface and bulk (Ru_i-Ru_b); (ii) interface distance; (iii) distance between opposite Si atoms on top ($Si_t - Si_t$), and bottom ($Si_b - Si_b$) faces; (iv) distances between opposite O atoms on top ($O_t - O_t$), middle (O_m-O_m), and bottom ($O_b - O_b$).

Table S3. Changes in distances of opposite Si and O atoms in flat silica nano-cage/Ru(0001) upon Xe trapping.

$\Delta d(Si_t-Si_t)$ (Å)	$\Delta d(Si_b-Si_b)$ (Å)	$\Delta d(O_t-O_t)$ (Å)	$\Delta d(O_b-O_b)$ (Å)	$\Delta d(O_m-O_m)$ (Å)
-0.09	-0.09	-0.39	-0.40	-0.19
-0.07	-0.08	0.38	0.38	-0.19
0.33	0.33	0.34	0.34	0.15

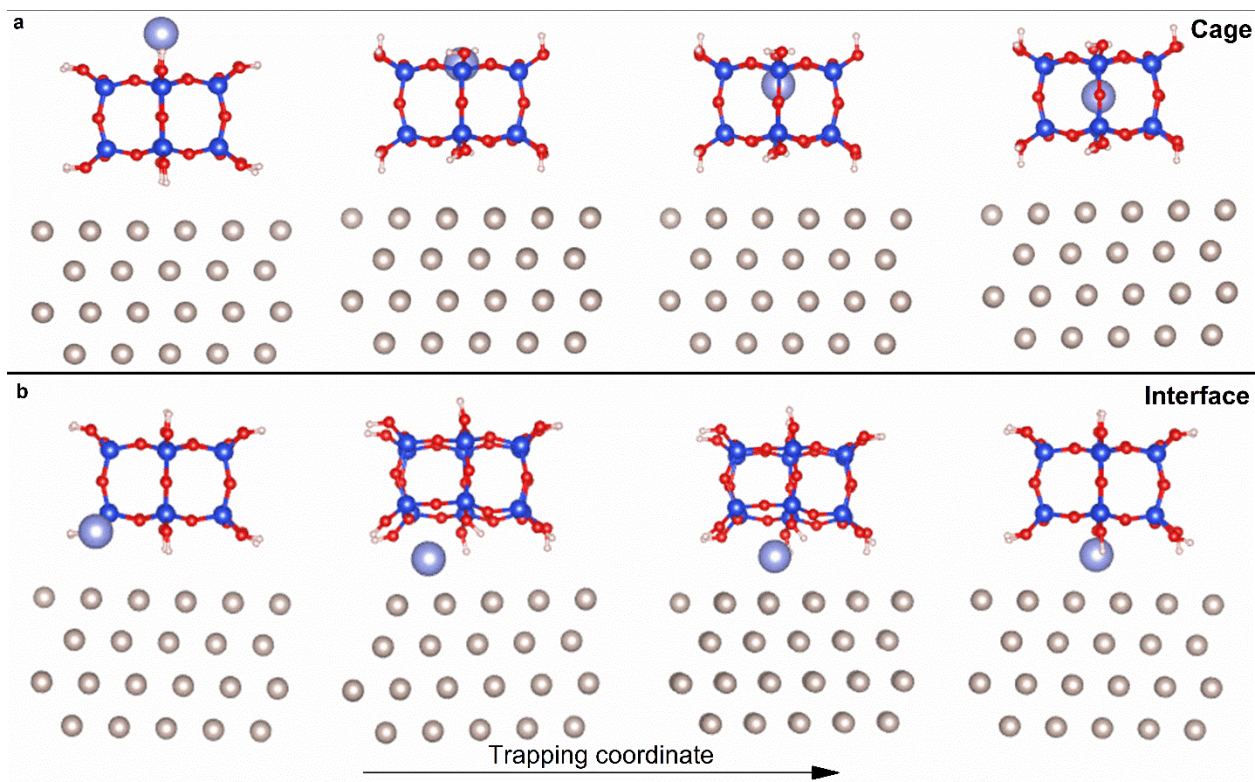


Figure S14. Schematic of silica nano-cage geometries used to simulate Xe trapping. **(a)** Inside a flat cage, and **(b)** at the interface between the cage and the Ru surface. From left to right, the trapping coordinate is shown (from adsorbed to trapped state). Careful inspection of the images indicates that as Xe enters the cage, Si and O move slightly to accommodate the noble gas's insertion.

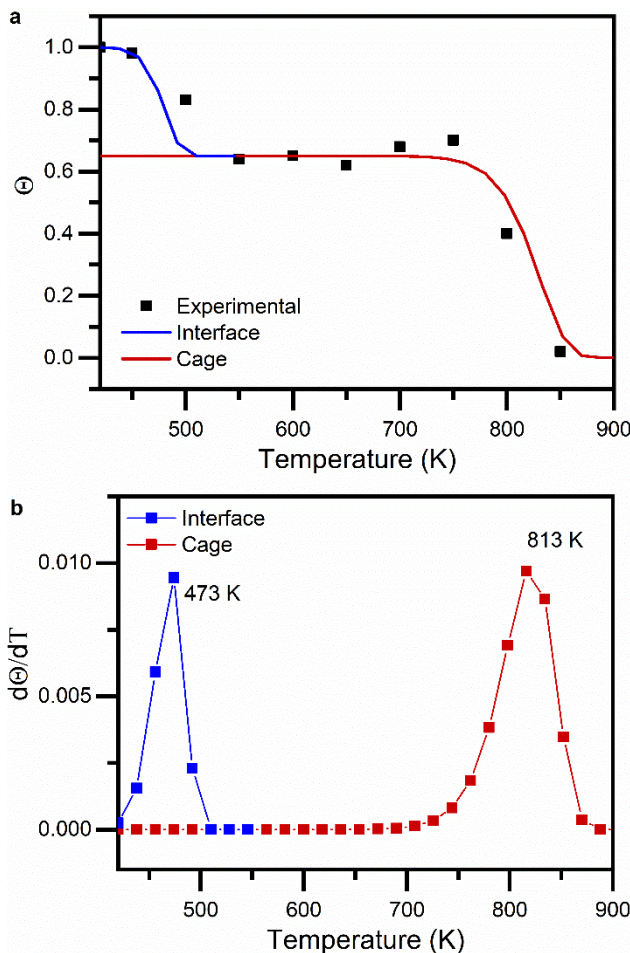


Figure S15. Simulated temperature-programmed desorption curve for Xe in the silica nanocages at different configurations: a flat cage with Xe trapped inside (dark red) and a flat cage with Xe trapped at the interface (blue). The intensity is calculated based on the first-order reaction law $\theta = \theta_0 \exp(-kt)$. The release rate constants (k) were calculated based on the Arrhenius equation $k = A \exp(-E_{rel}/(k_b T))$. The temperature is increased linearly, with a rate of 0.3 K/s.

Table S4. DFT calculated release energy barriers (E_{rel}) with ZPE correction.

Structure	T(K)	$\Delta S/k_B^*$	E_{rel}
Interface	473	-0.47 ± 0.22	1.27
Cage	813	-0.69 ± 0.28	2.36

* ΔS is defined as the difference between the entropy at the transition state and the entropy at the trapped state. S is a function of the temperature. The values are an average with the corresponding deviation in the temperature range evaluated.

Table S5. Core-level binding energy shifts for flat and anchored silica nanocages/Ru.

Structure	Xe 3d	Si 2p	O 1s
Interface	0.04	-	-
Anchored nanocage*	0.11	0.58	0.66

Corrected to the Fermi level and compared to the binding energy value of the flat nanocage.

*Using the transition-state approximation.

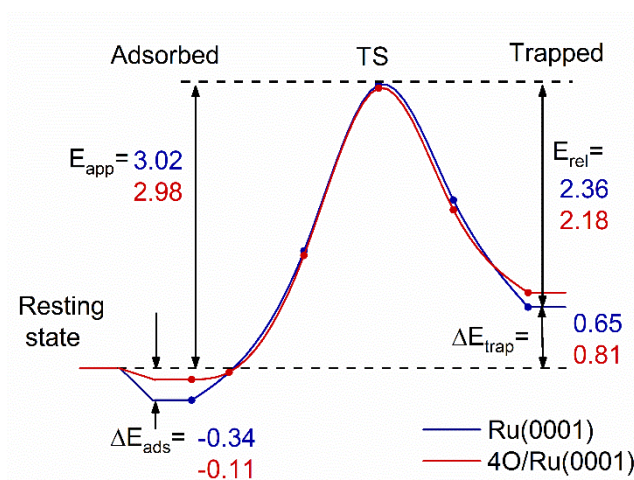


Figure S16. Potential energy diagram for Xe trapping on a flat silica nanocage: supported on a bare ruthenium surface (navy) and with chemisorbed oxygen ($\theta=0.25$) on ruthenium (red).

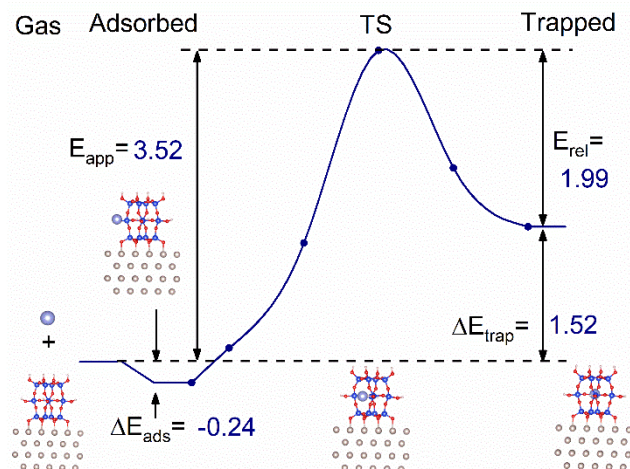


Figure S17. Potential energy diagram for Xe trapping on an anchored silica nanocage supported on a bare ruthenium surface.

Table S5. Changes in distances of opposite Si and O atoms in anchored silica nanocage/Ru(0001) upon Xe trapping.

$\Delta d(\text{Si}_i\text{-Si}_i)$ (Å)	$\Delta d(\text{Si}_b\text{-Si}_b)$ (Å)	$\Delta d(\text{O}_i\text{-O}_i)$ (Å)	$\Delta d(\text{O}_b\text{-O}_b)$ (Å)	$\Delta d(\text{O}_m\text{-O}_m)$ (Å)
-0.09	-0.10	-0.65	-0.66	-0.19
-0.10	-0.10	0.63	0.63	-0.19
0.65	0.67	0.62	0.62	0.43